ELECTRONIC INTERACTIONS BETWEEN GOLD FILMS AND MN_{12}–ACETATE

A Dissertation

by

JOEL LEWIS MEANS

Submitted to the Office of Graduate Studies of
Texas A&M University
in partial fulfillment of the requirements for the degree of

DOCTOR OF PHILOSOPHY

December 2007

Major Subject: Physics

ELECTRONIC INTERACTIONS BETWEEN GOLD FILMS AND MN_{12}–ACETATE

A Dissertation

by

JOEL LEWIS MEANS

Submitted to the Office of Graduate Studies of
Texas A&M University
in partial fulfillment of the requirements for the degree of

DOCTOR OF PHILOSOPHY

Approved by:

Chair of Committee,	Winfried Teizer
Committee Members,	Donald Naugle
	Artem Abanov
	Kim R. Dunbar
Head of Department,	Edward S. Fry

December 2007

Major Subject: Physics

ABSTRACT

Electronic Interactions Between Gold Films and Mn_{12}–Acetate. (December 2007)

Joel Lewis Means, B.S., Harding University

Chair of Advisory Committee: Dr. Winfried Teizer

Interactions between Mn_{12}–acetate molecular magnets and thin gold films have been explored in light of the theory of weak localization. Low-temperature measurements of the magnetoresistance of gold films of varying thicknesses, with and without the presence of a surface layer of Mn_{12}–acetate, have been performed using a dilution refrigerator. Quantitative fits to the data using the predictions of weak localization theory were performed using a least-squares fit method in order to determine characteristic times for elastic, inelastic, spin-orbit and spin scattering events within the gold. These data indicate that the presence of Mn_{12}–acetate on the surface of the gold film leads to a significant enhancement of the spin scattering within the gold films.

ACKNOWLEDGEMENTS

First and foremost, I must acknowledge the love and support of my wife and children, without which I would not have been able to complete this dissertation and my degree. Next I must give great thanks to Dr. Winfried Teizer, my advisor and friend. Without his guidance and encouragement, I would not have completed graduate school. I also need to thank Dr. Dave Toback, who gave me much needed words of encouragement early on in graduate school. Thanks are also due to Kyongwan Kim for so much help and assistance with the dilution refrigerator. Thanks go to all of my committee members for their assistance and guidance. Dr. Glenn Agnolet also deserves thanks for guidance and help. I also thank Dr. Valery Pokrovsky for serving on my advisory committee until a last minute substitution was necessitated.

TABLE OF CONTENTS

LIST OF FIGURES

FIGURE Page

LIST OF TABLES

CHAPTER I

INTRODUCTION

Manganese-12 acetate (Mn_{12}-ac), $[Mn_{12}O_{12}(CH_3COO)_{16}(H_2O)_4]\cdot 2CH_3COOH\cdot 4H_2O$, has been studied extensively over the past few years due to its many interesting magnetic properties. It was first synthesized by Lis [1] in 1980 and has received much attention, both theoretical [2–12] and experimental [13–19], since the early 1990's. While it is not a central theme of this study, one of the major attractions of Mn_{12} is the fact that quantum tunneling of the magnetization (QTM) [16] can be demonstrated on the macroscopic level. Generally, quantum effects are masked in bulk matter due to statistical averaging of the phenomena. Superconductivity and superfluidity in helium are two other examples of quantum effects which are manifested macroscopically. The discovery of fast magnetic relaxation at temperatures in the Kelvin range in single crystals of rare-earth intermetallics prompted the earliest research into magnetic quantum effects on the macroscopic scale [20]. Major problems with these studies arose from the fact that the crystals had a broad distribution of sizes, energy barriers and fields. One of the advantages of studying Mn_{12} and similar nanomagnets is the ability to synthesize molecules of identical size and properties, which enables precise characterization of the molecules [21]. In chapter II, the structure of the Mn_{12}-ac molecule will be discussed and an overview of its interesting magnetic properties will be given. Experimental evidence for the quantum tunneling of magnetization will be presented along with an explanation of the mechanisms of QTM in Mn_{12}-ac and similar clusters.

Most of the study up to this point on Mn_{12}–ac has been into its magnetic properties. A few reports on the electronic properties of Mn_{12}–ac have been made, mostly concerning conductance through the molecules [22–26]. There have also been reports on the electronic

---

This dissertation follows the style of Physical Review Letters.

structure of various Mn_{12} derivatives [5, 27]. The purpose of this thesis, then, is to offer some insight into the electronic structure of Mn_{12}-ac by exploring how these molecular magnets interact electronically with gold films. Specifically, this thesis will discuss the effects of placing a thin film of Mn_{12}–ac on the surface of a thin film of gold by looking at how the presence of the Mn_{12}–ac affects the magnetoresistance of the gold.

In order to understand the effects which a surface layer of Mn_{12}–ac can have on the electronic properties of a thin gold film, one must have a theoretical framework for explaining the possible interactions. This framework is provided by the theory of weak localization, which allows determination of the strength of various scattering interactions from measurement of the magnetoresistance of a material. Chapter III will explore the basic concept of magnetoresistance from a classical standpoint, followed by the quantum corrections to the resistance which arise from weak localization.

A major step required for this research was the deposition of thin films of Mn_{12}–ac. Due to the thermal instability of the Mn_{12}–ac molecules, typical techniques, such as thermal evaporation, used for deposition of thin metallic films, are not feasible. Various techniques have been used to create these films of Mn_{12}–acetate [28–30], including a Langmuir-Blodgett technique [31]. In our lab, we have developed two simpler methods. The technique in which the author has been involved is based on a technique that has become popular more recently. Pulsed laser deposition (PLD) has been used extensively for the deposition of organic and inorganic thin films [32]. We apply this method to produce films of Mn_{12}–acetate which maintain many of the magnetic and molecular properties of the crystalline starting material [33–35]. The other technique is a very simple dip-and-dry (and a variant, the drop-and-dry) technique [36, 37]. Both of these techniques will be described in chapter IV.

The low-temperature nature of the Mn_{12}–ac molecular magnets necessitates the use of a cryostat to perform the measurements. The fact that the changes in magnetoresistance

due to weak localization effects are very small requires very low temperatures in order to reduce noise levels. For these reasons, a dilution refrigerator was used for the measurements. Much effort was required to restore a home-built dilution refrigerator which had not been used in several years and for which very little documentation was available. Through the course of my study, I have learned the physics behind the function of the dilution refrigerator as well as the practical operation of the system. These aspects of the work will be outlined in chapter V.

Finally, chapter VI will discuss the experimental procedures used to measure the desired effects. Pertinent data is shown and discussed with connections made to the theory of weak localization.

CHAPTER II

Mn_{12}–ACETATE PROPERTIES

Chemical and Magnetic Properties

The Mn_{12}-ac complex is prepared by mixing $KMnO_4$ and $Mn(CH_3CO_2)_2{\cdot}4H_2O$ with a molar ratio of 1:2.5 in a 60% solution of acetic acid. The manganese atoms within the Mn_{12}-ac molecule are arranged in two shells (see Figure 1). The inner shell consists of four $Mn^{(IV)}$ ions with spin $S = \frac{3}{2}$ arranged in a cubane structure with four oxygen atoms. The outer shell is made up of eight $Mn^{(III)}$ ions with spin $S = 2$. The outer shell is linked to the inner by eight μ_3-O^{2-} anions. There are three different interaction energies between the Mn atoms which range in strength from 45 K to 215 K [38]. The spins of the inner ions are aligned to give a spin of $S = 6$, while the outer ions contribute a spin of $S = 16$. The inner shell and outer shell are antiferromagnetically coupled to give a total spin for the molecule of $S = 10$ in the ground state. This gives a net magnetic moment of $M = gS\mu_B \approx 20\mu_B$ ($g \approx 2$ is the Lande factor) [38].

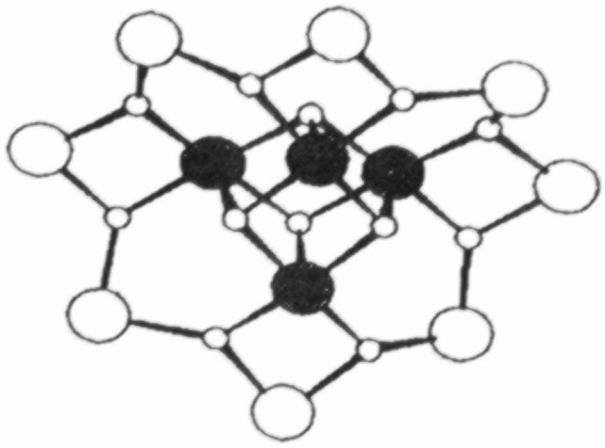

Figure 1: Mn_{12}–ac core structure. Large white circles denote Mn^{4+} ions, while the black ones denote Mn^{3+} ions. Small circles denote oxygen atoms.

Upon crystallization, the Mn_{12} clusters have a tetragonal symmetry with $a = 17.319$ Å and $c = 12.388$ Å [1], yielding a unit cell volume of 3716 Å^3 [15]. The average spacing of the Mn atoms is 15 Å. The crystal has two Mn_{12} molecules per unit cell along with waters and disordered acetic acid molecules. Jahn-Teller distortions lead to a strong axial anisotropy which forms a tunneling barrier between the $m = 10$ and $m = -10$ states [39]. The strength of this anisotropy barrier is approximately $61 - 65$ K [38]. The barrier arises from the fact that the Mn_{12}–ac molecules cannot physically rotate within the crystal lattice. Without Jahn-Teller distortions, one could imagine a roughly spherical molecule. In the presence of an external magnetic field, the molecule would be able to physically rotate within the lattice to align itself with the magnetic field. There would be essentially no barrier to transitions from one magnetic state to another. However, because of the Jahn-Teller distortions, the Mn_{12}–ac molecules are shaped more like a pancake. Within the crystal lattice, there is a physical barrier to rotation of the molecules, leading to the energy barrier that must be overcome for a magnetic transition from an $m = +10$ state to an $m = -10$ state.

In the crystalline state, there is little interaction between neighboring molecules. This is indicated by exploring the inverse of the dc susceptibility as a function of temperature. Above 3 K, the relation is linear, showing a Curie-Weiss behavior with $\theta \sim 70$ mK. This small amount of ferromagnetic coupling is possibly due to dipole-dipole interactions [38]. Other susceptibility measurements indicate a superparamagnetic effective moment of 20.4 μ_B at 10 K [19], in reasonable agreement with predictions. Above 10 K, this effective moment decreases due to the presence of the $S = 9$ and lower states.

Magnetization and electron paramagnetic resonance measurements indicate that the complex has a ground state spin along the easy axis (c-axis) of $m = \pm 10$ [39]. The complex shows superparamagnetic behavior as indicated by measurements of the magnetization, the specific heat and the complex susceptibility [19]. The magnetization shows

strong hysteresis below the blocking temperature of 3 K [17]. Steps which appear in the hysteresis are one indication of quantum tunneling of the magnetization [21] and will be discussed later. There is a splitting of the field cooled and zero field cooled curves below 3 K. This is an indication of blocking of the superparamagnetic particles [19]. At 4.2 K, the magnetization for a single crystal has been shown to saturate in a field of 20 kOe to a value of 20 μ_B [19], in agreement with theory and with susceptibility measurements mentioned above. Measurements of the complex AC susceptibility indicate a single relaxation time for the magnetization down to 2.1 K. This relaxation obeys the Arrhenius law $\tau = \tau_0 e^{(KV/k_B T)}$, where KV/k_B is the anisotropy barrier, and $\tau_0 \approx 2.6 \times 10^{-6}$ seconds for $T > 2.5$ K. Below 2.1 K, the relaxation time saturates at a value on the order of $10^7 - 10^8$ seconds, independent of temperature [17]. This behavior is also attributed to quantum tunneling of the magnetization and will be discussed in more detailed below.

Quantum Tunneling of the Magnetization

The process of quantum tunneling of the magnetization (QTM) was first considered theoretically in the 1980's [40–42]. Examples of QTM include magnetization tunneling between easy directions in a single-grain ferromagnetic particle [40] and domain wall tunneling through small pinning barriers in ferromagnets [43]. Early experimental work showed that many magnetic systems showed relaxation times on the order of days or months. This can only be explained as the decay of metastable states [44]. QTM has been shown in Co, Ni and CoZrMoNi samples through the demonstration of square hysteresis loops at low temperature (between 0.1 K and 5 K) [15]. The sharp transition in the magnetic moment cannot be attributed to rotation of the particles since they are too large for simultaneous rotation throughout the sample.

As previously mentioned, one indication of the presence of QTM in Mn_{12}-ac is the presence of discrete, regularly-spaced steps in the hysteresis loops. Friedman *et al*. [21], have found steps in the hysteresis loops with a spacing of 0.45 T. It was found that the relaxation time, τ, for the magnetization was much longer than the experimental time frame (on the order of 600 seconds) in the flat regions (out of resonance) while in the steep regions (at resonance), the relaxation was much faster, within the experimental time frame [38]. This is evidence of field-tuned resonant tunneling between spin states in a large number of identical high-spin molecules.

The field dependence of the relaxation time has been studied by Paulsen *et al*. [17], who found that $\tau(H)$ has a deep minimum below a critical temperature of 2 K in zero field, while above 2 K, it has a maximum at 0.2 T. This behavior has been attributed to increased tunneling of the $S = \pm 10$ states due to a resonant energy-level crossing in a two-well potential. Support for this idea comes from the fact that the thermal energy corresponding to this field of $H_m = 0.2$ T is $\frac{3}{2}k_BT = 20\mu_B H_m = 2$K, which is the critical temperature. In a typical superparamagnet, τ shows a monotonic decrease with increasing field. This is due to the fact that increasing the field lowers the anisotropy energy barrier. As a result of QTM, Mn_{12}-ac samples show a maximum in the relaxation time at 1.5 kOe and two separate minima at 4.5 kOe and 8.5 kOe [45].

Friedman *et al*. [21], also found that at lower temperatures, steps which occur at high field are more evident while low field steps are not apparent. At higher temperatures, this is reversed, with the low field steps becoming more evident. This is due to the change in the relaxation times with temperature. The field changes faster than the system can react at low temperature, effectively "freezing out" some of the steps. Slowing down the sweeping rate for the field allows more steps to be seen [21].

The temperature dependence of the relaxation rate has also been explored. Above 2.5 K, the relaxation rate has been shown to be a single exponential on the order of 10^{-5}

seconds. As the temperature decreases, this behavior shifts to a constant on the order of $10^7 - 10^8$ seconds [16]. This value is obviously outside of the experimental time frame and is deduced from an expansion of the exponential term in equation 1 (below), which gives the magnetization as a function of time. This expansion shows that the slope of the M vs. t graph is well approximated by $1/\tau$. τ can then be calculated from data taken for a smaller amount of time. As stated previously, this long relaxation time can only be explained as the decay of a metastable state. This decay is understood as QTM, as explained below.

It has been shown that the blocking temperature, T_B, which is the temperature where the thermal energy is equal to the anisotropy energy, is lowered as the magnetic field used for measurement is increased [21]. The magnetization of a Mn_{12}-ac sample was measured as a function of temperature in fields ranging from 0.6 T to 1.2 T. The samples were cooled in zero field to 1.7 K and measured as the temperature was raised. The blocking temperature was determined as the maximum in the magnetization curve. As the measurement field was increased, the blocking temperature was steadily lowered, as expected. An anomaly was found in the curve for $H = 0.9$ T. This curve crossed the 1.0 T curve and showed a lower blocking temperature as well as a sharper drop in the magnetization below T_B.

Further investigation of this dip in the relaxation time at 0.9 T was carried out by Friedman *et al*. [21]. The deviation of the magnetization from its asymptotic value as a function of time was determined for a sample cooled to 2.4 K at zero field and then measured in fields of 0.9 T and 0.95 T. An exponential fit to the data was done with the first ~2000 seconds omitted, from which M_0 was calculated. A faster decay seen during the first 2000 seconds is not understood. Data indicate that the deviation from M_0 occurs much faster for $H = 0.9$ T. The data show an exponential decay after the first 2000 seconds given by

$$M = M_0 \left(1 - e^{-(t-t_0)/\tau}\right) \tag{1}$$

The respective time constants for 0.9 T and 0.95 T are found to be 1048 sec^{-1} and 2072 sec^{-1}. The much faster decay at 0.9 T is strong evidence of a QTM resonance.

Determination of T_B as a function of the applied field, H, indicates distinct dips at the same field values for which the steps occur in the hysteresis. Other measurements of the relaxation time as a function of field, carried out by Thomas *et al*. [46], have shown oscillations with resonances at the same field values for which the steps in the hysteresis occur. Together, the steps in the hysteresis and the dips in the blocking temperature and relaxation rates indicate a sharp increase in the tunneling rate through the anisotropy barrier at these specific field values. This increase is a result of resonance tunneling.

All of the above properties were measured below the blocking temperature. Above this temperature, relaxation rates cannot be determined from magnetization measurements because the relaxation is too fast. For temperatures higher than the blocking temperature, AC-susceptibility measurements are used. The complex susceptibility is given by $\chi(\omega) = \chi'(\omega) - i\chi''(\omega)$ (where ω is the frequency of the AC field). The real and imaginary parts of the susceptibility are given by

$$\chi' = \chi_S + \frac{\chi_T - \chi_S}{1 + \omega^2\tau^2} \tag{2}$$

and

$$\chi'' = \frac{(\chi_T - \chi_S)\,\omega\tau}{1 + \omega^2\tau^2} \tag{3}$$

where $\chi_S = \chi_{\omega\to\infty}$ is the adiabatic susceptibility and $\chi_T = \chi_{\omega\to 0}$ is the isothermal susceptibility [18]. The relaxation time can be found from the fact that χ'' is a maximum when $\omega\tau = 1$. These measurements have shown oscillations with minima at the same field values found in low temperature measurements, but the amplitude of the oscillations was lowered.

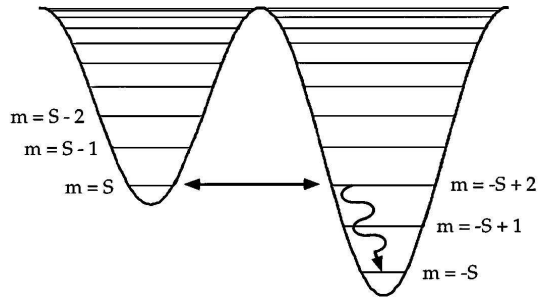

Figure 2: Double well potential at resonance. This represents a decay to the stable state $m = -S$ after a tunneling transition from $m = S$ (metastable) to $m = -S+2$. (Reprinted with permission from [21], Copyright 1996 by the American Physical Society.)

Theoretical explanation of these effects comes from exploring the Hamiltonian of the system. The simple Hamiltonian can be given as

$$\mathcal{H} = -DS_z^2 - \mu_B \overrightarrow{S} \cdot \overrightarrow{H} \tag{4}$$

where D is the anisotropy energy constant of 0.56 K.

This system can be modeled by a double well potential. At zero field, the two wells are symmetric and the $m = \pm S$ ground states are degenerate. Application of an axial magnetic field shifts the energy of the two states in opposite directions. If the field is applied anti-parallel to S, then the energy of the $m = S$ state is raised and the $m = -S$ state becomes the true ground state (see Figure 2). If the system is initially placed in the $m = S$ ground state, application of the field shifts the system to a metastable state. Without tunneling, transition from one state to another can only take place through thermal excitations over the barrier. If tunneling through the barrier is allowed, it is inhibited by an applied field. At certain values of the magnetic field, however, one can tune the system such that the energy of two states on different sides of the barrier becomes degenerate. This degeneracy allows for a tunneling event which is followed by a fast transition down to the ground state. This tunneling leads to a drop in the relaxation time for the magnetization.

The state of a particle can be given by $|S, m>$. Assuming that the particle starts in the $|S, S>$ state, it will tunnel to the $|S, -S+n>$ state when those two states have the same energy. A simple calculation using the Hamiltonian of Equation 4 shows that this occurs at a field of

$$\mathcal{H}_{S,-S+n} = \frac{-Dn}{g\mu_B} \tag{5}$$

Using the given value of $D = 0.56$ K, this gives the $\mathcal{H}_{S,-S+n} = 0.42n$ T. This is in close agreement with the experimental observation that steps occur at regular intervals with a spacing of 0.45 T. It has also been found that when the system is tuned to resonance for one level in the left hand well, all of the levels are tuned, giving multiple resonant transitions [21]. It should be noted that no steps are seen in hysteresis loops as the field is decreased from the saturation field. This is due to the fact that at saturation, only the true ground state is populated. Tunneling does not occur until the field is reversed and the previous ground state becomes metastable.

Tunneling can only occur given non-zero matrix elements of $\mathcal{H}$ with states of different S_z. If H is directed axially, the given Hamilton (Equation 4) commutes with S_z and tunneling is not allowed. Tunneling must come from higher order perturbations due to an off-axis component of the magnetic field or to a transverse anisotropy within the crystal lattice. Including fourth order terms in the Hamiltonian, one can write

$$\mathcal{H} = AS_z^2 + BS_z^4 + C\left(S_+^4 + S_-^4\right) \tag{6}$$

where $A = -0.56$ K, $B = -1.1 \times 10^{-3}$ K and $C = 2.9 \times 10^{-5}$ K [45]. The last term in Equation 6 represents a weak transverse anisotropy. This basal plane anisotropy is what allows the tunneling to take place, but its origin in Mn_{12}-ac crystals is not well understood. In zero field, the transverse anisotropy terms remove the degeneracy of the

± 10, ± 6 and ± 2 levels. One major limitation of this Hamiltonian, however, is that it only allows tunneling to occur between states with $\Delta m_s = \pm 4n$, where n is an integer [45]. Experimentally, transitions are seen for all values of Δm_s up to at least 11 [39], although it has been suggested that 21 such transitions should be seen [47]. Work is currently being done to try to understand these transitions in light of quantum noise in Landau-Zener transitions [48].

The Hamiltonian of Equation 6 is based on the model of the Mn_{12}-ac being in a collective spin $S = 10$ state. Validity of this Hamiltonian must then be limited by the validity of the $S = 10$ model. To determine the temperature range of validity, one can calculate the energy levels of the system based on the binding energies given by Tupitsyn and Barbara [38]. The Hilbert space for this problem has dimension 10^8. Tupitsyn and Barbara have suggested that reduction of the problem can be achieved by assuming that, below 150 K, two Mn ions with $S_1 = 2$ and $S_2 = 3/2$ can be viewed as a single particle in a state with $S_{12} = 1/2$ due to the strong coupling (on the order of 200 K) between them. This leads to an effective eight-spin Hamiltonian given by

$$\mathcal{H} = \frac{1}{2}\left[\sum_{\langle\mu,\nu\rangle}^{4}\left(C_1 S_\mu \sigma_\nu + C_\parallel S_\nu^z \sigma_\mu^z\right) + C_2 \sum_{\langle\alpha,\beta\rangle}^{4} \sigma_\alpha \sigma_\beta\right] + g\mu_B H \cdot \left(\sum_{\mu=1}^{4} S_\mu + \sum_{\nu=1}^{4} \sigma_\nu\right) \quad (7)$$

where $S = 2$ and $\sigma = \frac{1}{2}$ denote the four outer shell ions and the four strongly coupled pairs, respectively. Solution of this Hamiltonian can be done in a Hilbert space of dimension 10^4, which is calculable. The Hamiltonian of Equation 7, while reduced, still contains the anisotropy and exchange energies and models the Mn_{12}-ac molecule well. Tuning of the coupling constants was done through comparison with experimental results. This Hamiltonian, with values of $C_1 = -85$ K, $C_2 = 55$ K and $C_{||} = -7.5$ K, has been shown to accurately predict the magnetization and susceptibility in a transverse field below 150 K [38]. Above 150 K, the coupling between the $S = 2$ and $S = \frac{3}{2}$ molecules breaks

down and the reduced Hamiltonian is no longer valid. Tupitsyn and Barbara have been able to use this Hamiltonian to find that the collective spin $S = 10$ model is valid up to 40 K. At 40 K, the $S = 9$ state becomes occupied. Above 40 K, however, the tunneling rate for the $S = 10$ state is still much faster than that of the $S = 9$ state due to the fact that the tunneling barriers for the lower spin states are higher and broader. AC susceptibility measurements lend experimental support to this by showing that the resonances are still evenly spaced above 40 K rather than being randomly spaced [38].

Tupitsyn and Barbara have also set forth the idea of an "effective barrier" height [38]. This "effective barrier" is the height of the lowest energy level where the tunneling can be measured experimentally. Above this level, tunneling is too fast to be measured due to the larger tunnel splitting. In zero field, the "effective" height is found to be $E_{eff}(0) = D\left(S_z - m_t\right)^2$, where m_t is that lowest energy level. In a non-zero field, the height is found to be $E_{eff}(H) = -E_{eff}(0) \cdot \left(1 + \frac{H_z}{2DS}\right)^2$ assuming $S \gg 1$ and dropping higher order terms. The estimated value of m_t was found to be $\sim 3 - 4$ [20].

Experimental evidence that quantum effects can be manifested at the macroscopic level has sparked much research into the topic over the past several years. Nanomagnets, such as the Mn_{12}-acetate complex, offer great opportunities for the study of one of these phenomena, quantum tunneling of the magnetization, due to the ability to fabricate these materials with little to no distribution in the size and magnetic properties of the molecules. Experimental evidence and theoretical explanation of QTM within the Mn_{12}-ac complex have been presented in this chapter. The field and time dependence of the magnetic relaxation times, steps occurring in the magnetic hysteresis loops and the field dependence of the blocking temperature are all evidence of QTM in Mn_{12}-ac. The problem can be understood theoretically as thermally assisted tunneling of the magnetization through the anisotropy barrier in a double well potential. Further research should continue to yield a better understanding of macroscopic quantum effects.

CHAPTER III

WEAK LOCALIZATION THEORY

Classical Magnetoresistance

Magnetoresistance is a phenomenon in which the resistance of a metal changes with increasing magnetic field [49]. It can be understood through a discussion of the motion of charge carriers in mixed electric and magnetic fields. Assume a conducting wire is oriented along the x-axis. An electric field is applied in the $+x$ direction, leading to a current. A magnetic field $\overrightarrow{H}$ is applied in the $+z$ direction. If we assume a single carrier type in the metal, then the velocity of the charge carriers is determined by equation 8:

$$\overrightarrow{v} = \frac{e\tau}{m^*}\left(\overrightarrow{E} + \left(\frac{1}{c}\right)\overrightarrow{v} \times \overrightarrow{H}\right) \tag{8}$$

where τ is the characteristic scattering time of the charge carriers, and m^* is their effective mass. The current density in a given direction is related to the electric field through the conductivity tensor, $\overleftrightarrow{\sigma}$ as $j_\lambda = \sigma_{\lambda\nu}E_\nu$. Solving equation 8 for the motion of the carriers, the conductivity tensor is found to be:

$$\overleftrightarrow{\sigma} = \frac{ne\mu}{1+\xi^2}\begin{pmatrix} 1 & \xi & 0 \\ -\xi & 1 & 0 \\ 0 & 0 & 1+\xi^2 \end{pmatrix} \tag{9}$$

where $\mu = \frac{e\tau}{m^*}$ and $\xi = \frac{\mu H}{c}$ are used to simplify the expression. The selected geometry means that $j_y = 0$, from which it follows that $j_x = ne\mu E_x$ and that $E_y = \xi E_x$. So we see that the current is independent of the magnetic field in the case of a transverse magnetic field. Experimental evidence shows that this is not the case for most metals [49], including gold, so the assumption of a single carrier type must be incorrect.

So we must turn our discussion to the situation involving two carrier types. We now have two equations of motion, one for each carrier type. They are:

$$\overrightarrow{v_1} = \frac{e\tau_1}{m_1^*}\left(\overrightarrow{E} + \left(\frac{1}{c}\right)\overrightarrow{v_1} \times \overrightarrow{H}\right) \tag{10}$$

$$\overrightarrow{v_2} = \frac{e\tau_2}{m_2^*}\left(\overrightarrow{E} + \left(\frac{1}{c}\right)\overrightarrow{v_2} \times \overrightarrow{H}\right) \tag{11}$$

In the high field limit (where $|\omega_{c1}\tau_1| \gg 1$ and $|\omega_{c2}\tau_2| \gg 1$, with ω_{ci} the cyclotron frequency of the i^{th} carrier type), the equations of motion can be simplified to $E_x + \left(\frac{H}{c}\right) v_{1y} = 0$ and $E_x + \left(\frac{H}{c}\right) v_{2y} = 0$. The transverse conductivity is then $\sigma_{yx} = (n_1 - n_2)\left(\frac{ec}{H}\right)$. For equal numbers of the two carrier types ($n_1 = n_2$), we find that $\sigma_{yx} = 0$ and $E_y = 0$ so that the resistivity is simply $\rho = \frac{1}{\sigma_{xx}}$ where $\sigma_{xx} \approx \left(\frac{n|e|}{H^2}\right)\left(\frac{1}{|\mu_1|} + \frac{1}{|\mu_2|}\right)$. Here we see that if the numbers of the two carrier types are equal, the transverse magnetoresistance increases as H^2 and does not saturate.

In the case when the numbers of carrier types is not equal, the magnetoresistance tends to saturate in all but some certain crystal orientations. This is understood as being due to open orbits, which carry current only in one direction in high magnetic fields. These open orbits keep the magnetoresistance from saturating in that direction. It can be shown [50] that the magnetoresistance will saturate unless the open orbits carry current in the y-direction.

For polycrystalline films, however, the situation is different since one cannot define crystal axes for the entire sample. P. Kapitza showed [49] that the magnetoresistance for polycrystalline films of most metals follows an H^2 curve for small H and becomes linear in H for larger H. The transition from quadratic to linear behavior varies by material and was found to occur anywhere from 0.5 T to 25 T. The transition is also affected by the

purity of the metal being studied. For Au, it was shown to range from 5 T to 12 T, with a lower purity leading to a higher transition.

Weak Localization

The preceding discussion of magnetoresistance is based on classical transport theory. When quantum effects are included in the discussion, correction terms must be added. These quantum corrections to the resistivity of metals are explained by the theory of weak localization. Weak localization was first proposed by Abrahams, et al., in 1979 [51]. Much theoretical work followed (for a theoretical review see ref. [52]). Notably, Hikami, et al. [53], set forth corrections which included spin-orbit coupling, greatly improving the theory's ability to explain some experimental results which were not in line with theory up to that point. An excellent review of the theory with emphasis on connections to experimental results was presented by Bergmann in 1983 [54].

To explore weak localization, one must look at what happens to an electron propagating within a metal. An electron will move in a random-walk pattern, undergoing various scattering processes within the lattice. The electron has a certain probability of following a given path and returning to where it started. Classically, the electron has the same probability of following the same path in reverse in order to return to its starting point. The probability density of finding the electron at a given distance from its starting point at a given time is then simply given by the classical diffusion equation:

$$p\left(r,t\right)=\left(\frac{1}{4\pi Dt}\right)e^{-\frac{r^2}{4Dt}} \tag{12}$$

where D is the diffusion constant of appropriate dimensionality.

Quantum mechanically, though, one cannot view the electron as simply following a given path. It must be viewed as a sum of partial-waves following all possible paths. For

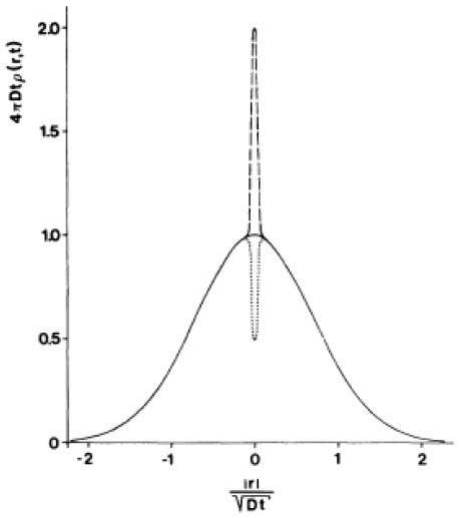

Figure 3: Probability distribution for the location of an electron diffusing within a metal. Solid curve shows classical diffusion, while dashed peak corresponds to quantum diffusion. Dotted peak shows situation for a system with a large spin-orbit coupling. (Reprinted with permission from [54], Copyright 1983 by the American Physical Society.)

one given path, one can look at the two partial-waves which follow the path in opposite directions. As long as the two partial-waves remain phase-coherent, they will interfere constructively at the origin, giving twice the classical probability of finding the electron back where it started (see Figure 3). This is what is known as weak localization and it manifests itself as an increase in resistivity.

In materials which exhibit a strong spin-orbit coupling, however, the case is different. The change in phases of the two partial waves due to the spin-orbit scattering leads to destructive interference at the origin which leads to a reduction in the probability of finding the electron there [55]. The probability is reduced by a factor of 2. This is known as weak antilocalization and gives a reduction in resistivity.

In the presence of a magnetic field, the two partial waves encircle some amount of magnetic flux in different directions, causing different phase shifts, depending on the path taken. This leads to a loss of phase coherence and weak localization (or anti-localization)

is diminished or completely broken. As Bergmann puts it, then, measurement of the magnetoresistance can be used as a "time-of-flight experiment" for the charge carriers in a metal. This means that the magnetoresistance data can be used to determine the characteristic scattering times of the material in question.

Theory predicts that the magnetoresistance of a 2D metallic film in a perpendicular magnetic field, $H_\perp$, can be written as [56]:

$$\frac{\Delta R\left(H_\perp\right)}{R} = \frac{e^2 R_\square}{2\pi^2\hbar}\times \tag{13}$$

$$\left[\psi\left(\frac{1}{2}+\frac{H_1}{H_\perp}\right)-\psi\left(\frac{1}{2}+\frac{H_2}{H_\perp}\right)+\frac{1}{2}\psi\left(\frac{1}{2}+\frac{H_3}{H_\perp}\right)-\frac{1}{2}\psi\left(\frac{1}{2}+\frac{H_2}{H_\perp}\right)\right]$$

where $R_\square$ is the sheet resistance of the film, ψ is the digamma function, and the characteristic fields, H_n, are given by

$$H_1 = H_0 + H_{so} + H_s \tag{14}$$

$$H_2 = \frac{4}{3}H_{so} + \frac{2}{3}H_s + H_i \tag{15}$$

$$H_3 = 2H_s + H_i \tag{16}$$

The strength of the various contributions to the magnetoresistance are given by the average time between scattering events of a certain type, τ_n. The characteristic fields are related to the scattering times by

$$H_n\tau_n = \frac{\hbar}{4eD} \tag{17}$$

The diffusion constant, D, is given in two dimensions as $D = \frac{1}{2}v_f^2\tau_0$ with v_f being the Fermi velocity. The subscripts denote elastic scattering, "0"; inelastic scattering, "i"; spin-orbit scattering, "so"; and spin scattering, "s". Thus, one can measure the magnetoresistance of a film and fit the curve using the above formulae to determine the characteristic scattering times of the material. The basic predictive ability of this formalism has been shown in many different types of experiments [56–64]. The results portion of the experimental chapter (chapter VI) will show fits for the collected data in line with the procedures used in these references.

Some discussion should be given to what these various scattering processes are. Elastic scattering events are those in which the energy and phase of the scattered electron remain unchanged. For example, scattering of an electron from lattice defects (missing ions or non-magnetic impurities) or from the surface (in two-dimensional systems) is an elastic scattering event. Inelastic scattering involves the loss of energy and a loss of phase coherence by the scattered electron. An example of inelastic scattering is electron-phonon scattering, where the electron absorbs or emits a phonon, changing its energy. Spin scattering would occur when a conduction electron scatters off of a magnetic impurity through a spin-spin interaction. Spin scattering events break the phase coherence between the incoming wave and the back-scattered echo. Spin-orbit scattering occurs when an electron moves in an electric field, $\overrightarrow{E}$. The spin angular momentum ($\overrightarrow{s}$) of the electron interacts with its orbital angular momentum ($\overrightarrow{L} = \overrightarrow{v} \times \overrightarrow{E}$, where $\overrightarrow{v}$ is the velocity of the electron). This scattering process changes the phase of the electron, but in a way that maintains phase coherence.

Figures 4, 5, 6, 7, and 8 illustrate the effects of changes to the different parameters on the magnetoresistance. Figure 4 was plotted with H_{so}=H_s=H_i=0. Increasing H_0 is seen to raise the curve. Figure 5 is the same as figure 4, except that H_{so} has been changed to a value of 1. This changes the magnetoresistance from negative to positive (as does

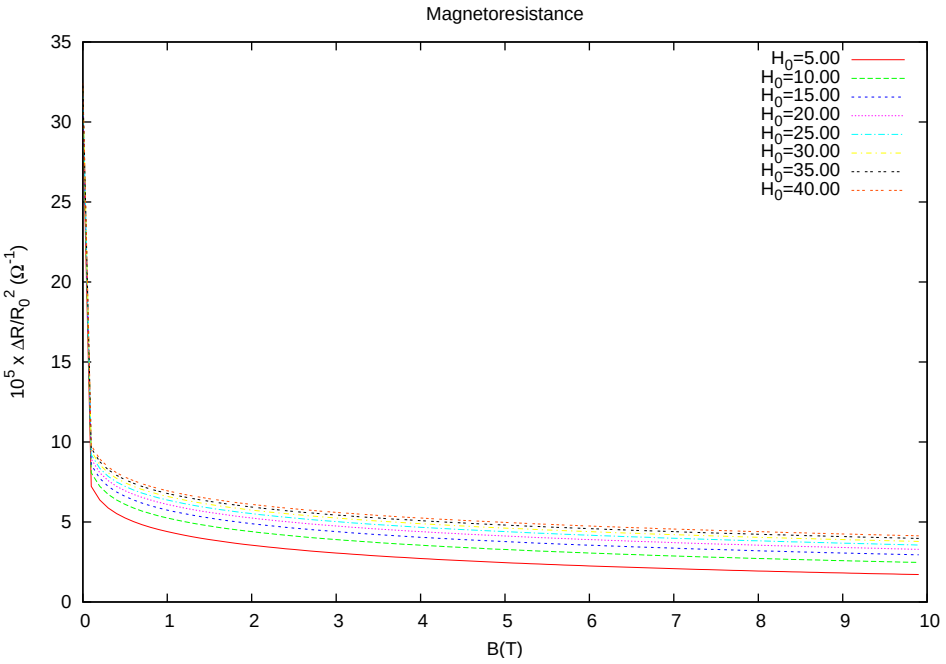

Figure 4: A series of magnetoresistance curves showing the effect of changing H_0, with H_{so}00. As H_0 is increased, with fixed H_{so}, H_s, and H_i, the curve moves up. With H_{so}=0, the magnetoresistance is negative.

any H_{so}>0). Figure 6 was plotted with H_0=10 and H_s=H_i=0. It is noted here that an increase in H_{so} leads to a raising of the curve. Also, as H_{so} is increased, the slope of the magnetoresistance curve above ∼2.5 T changes from positive to negative. Figures 7 and 8 were both plotted with H_0=10 and H_{so}=1 and the other non-variable parameter set to zero. Both show a broadening of the magnetoresistance curve with an increase in either H_s or H_i, respectively.

In a parallel magnetic field, $H_{\|}$,the magnetoresistance is given by [56]:

$$\frac{\Delta R\left(H_{\|}\right)}{R}=-\frac{e^{2}R_{\square}}{2\pi^{2}\hbar}\left[\frac{3}{2}\ln\left(1+\frac{L_{2}^{2}}{L_{\|}^{2}}\right)-\frac{1}{2}\ln\left(1+\frac{L_{3}^{2}}{L_{\|}^{2}}\right)\right] \tag{18}$$

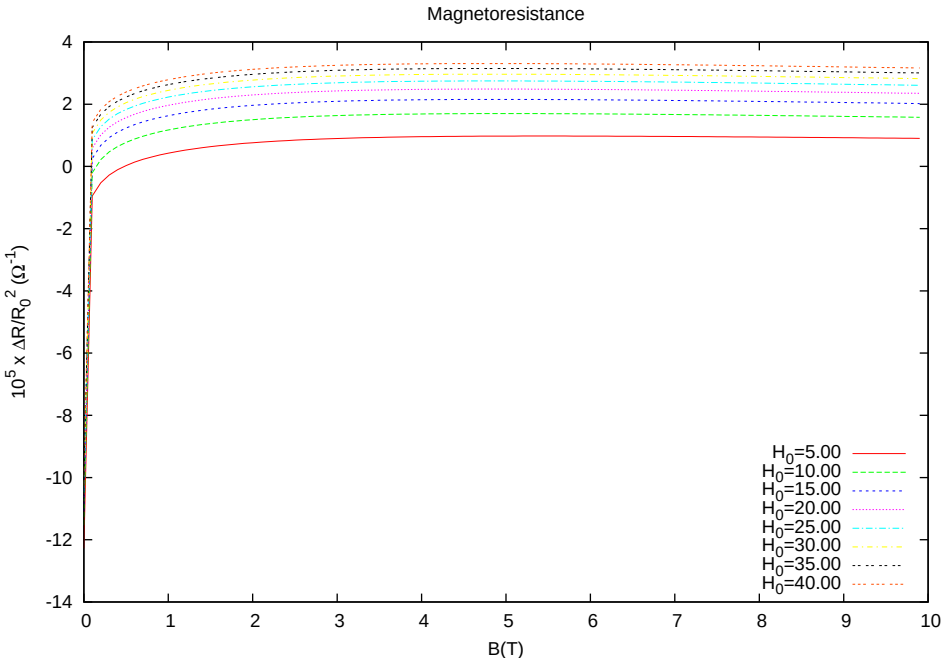

Figure 5: A series of magnetoresistance curves showing the effect of changing H_0, with H_{so}>0. As H_0 is increased, with fixed H_{so}, H_s, and H_i, the curve moves up. With H_{so}>0, the magnetoresistance is positive.

where L_2 and L_3 are defined by

$$L_n^2 = D\tau_n = \frac{\hbar}{4eH_n} \tag{19}$$

with the H_n given by equations 15 and 16. The value of $L_\parallel$ depends on the elastic mean free path, l, and thickness, t, of the film. The film can be considered in the "clean" ($t < l$) or "dirty" ($t > l$) limit, which are given by

$$L_\parallel = \sqrt{\frac{16l}{3t}}\frac{\hbar}{eH_\parallel t} \tag{20}$$

or

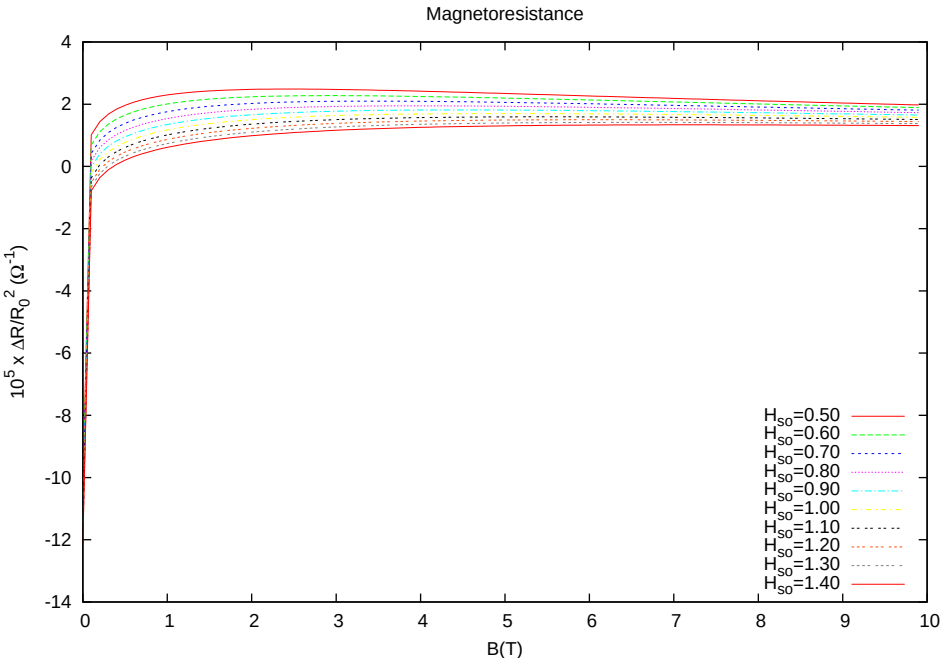

Figure 6: A series of magnetoresistance curves showing the effect of changing H_{so}. As H_{so} is increased, with fixed H_0, H_s, and H_i, the curve moves up and the slope of the curve above $\sim$2.5 T shifts from positive to negative.

$$L_{\parallel} = \frac{\sqrt{3}\hbar}{eH_{\parallel}t} \tag{21}$$

respectively.

Related to the present work, the effect of placing 3d, 4d and 5d atoms on the surfaces of thin films of noble metals has been studied, both theoretically [65] and experimentally [58, 59, 66]. The most pertinent of these results is work done by Beckmann, Ye, and Bergmann, exploring V atoms on Au surfaces [66], since V and Mn are both 3d atoms. It was found that as the coverage of V atoms is increased from $\frac{2}{100}$ of a monolayer up to 0.42 monolayers, the magnetoresistance curve is continually broadened, due to the enhanced

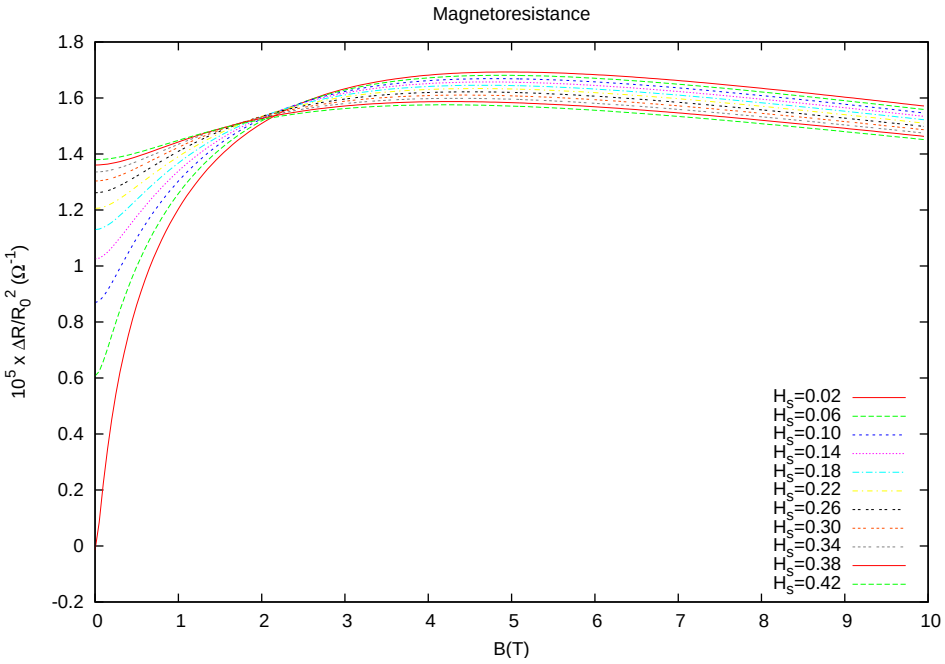

Figure 7: A series of magnetoresistance curves showing the effect of changing H_s. As H_s is increased, with fixed H_0, H_{so}, and H_i, the curve becomes more shallow.

spin scattering brought about by the 3d surface impurities. Above 0.42 monolayers, the curve begins to narrow again, due to a decrease in the magnetic moments of the V atoms with increased coverage. This paper also mentions an unpublished experiment exploring the effect of placing Mn atoms on a Au surface. In the case of Mn, it was found that the magnetoresistance curves broadened continuously with increased Mn coverage up to 0.1 monolayers, at which point the curve was so broad that it could no longer be evaluated. This is, however, for bare Mn atoms on a Au surface. One would expect the situation to be different for clusters involving one or several $Mn^{(III)}$ or $Mn^{(IV)}$ ions. In fact, in the case of Mn_{12}–ac, the presence of acetate ligands surrounding the magnetic core of the molecule would keep the Mn ions from coming into direct contact with the surface.

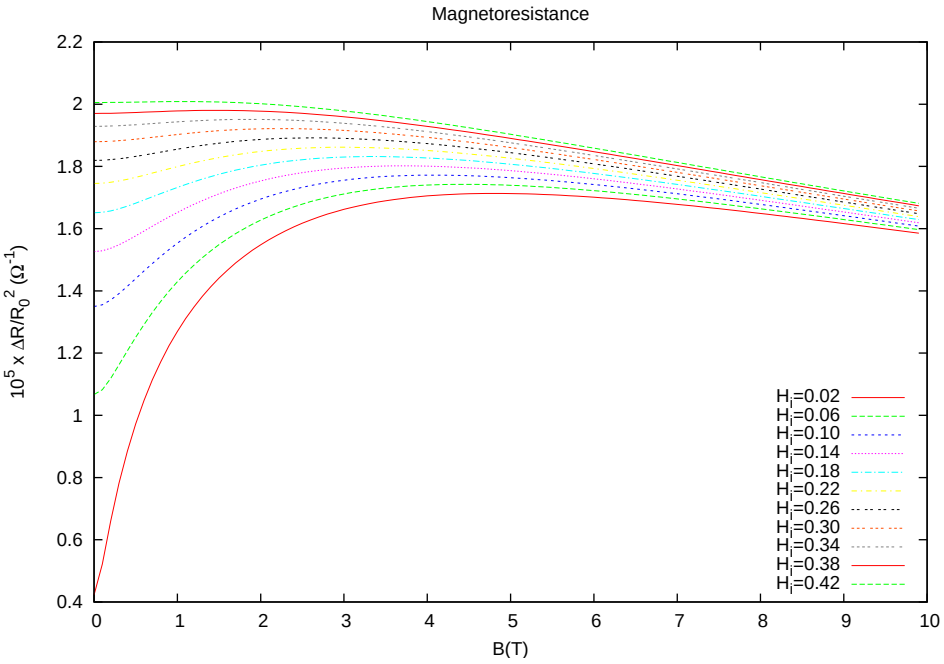

Figure 8: A series of magnetoresistance curves showing the effect of changing H_i. As H_i is increased, with fixed H_0, H_{so}, and H_s, the curve becomes more shallow.

CHAPTER IV

Mn_{12}–ACETATE THIN FILM CREATION

Pulsed Laser Deposition

Technique

Pulsed laser deposition involves ablating the source material with a laser, causing a plume of material to be expelled from the source and deposited on an adjacent substrate. The process we used for this is as follows. The Mn_{12}–ac is produced in the form of a crystalline powder. This cryatalline starting material is pressed into a pellet under a pressure of $\sim$19000 torr. The pellet is mounted in a high-vacuum chamber as the ablation target. Across from the target, at a distance of 2-3 inches, a substrate is mounted. In the initial studies of this technique, silicon (with the native oxide layer intact), mica, and glass were all used as deposition substrates. A quartz crystal microbalance is also mounted adjacent to the substrate for calibrated measurement of the film thickness. The chamber is then evacuated to a pressure of $\sim 5 \times 10^{-6}$ torr. The chamber is pumped to rough vacuum ($\sim$ 200 mT) using a Varian SD200 direct-drive mechanical pump before switching to a Pfeiffer Duo 1.5A turbo pump to reach lower pressures. The rough vacuum is measured with a thermocouple (TC) gauge while high vacuum is measured with a Bayer-Alpert type ion gauge. Both pressure gauges are controlled with a Varian model 843 vacuum gauge controller.

Two different lasers were employed for the ablation process. Early work was done using a Lambda Physik Compex 201 KrF Excimer laser. Laser energies ranging from 200 to 450 mJ were used. Partial fragmentation of the Mn_{12} molecules was observed in mass spectrometry data at higher energies [35]. Films made at lower energies exhibited less

fragmentation. Therefore, the author decided to pursue the use of a lower energy nitrogen laser.

The nitrogen laser used was a Molectron UV-22 pumped dye laser. Films were created using two different sets of deposition criteria. The first set used a pulse frequency of 8 Hz with a pulse energy of 0.8 mJ and a deposition time of 5.5 hours. The second set used a pulse frequency of 20 Hz, a pulse energy of 2 mJ and a deposition time of 3 hours. The ablated material was then characterized chemically and magnetically to see if it maintained the properties of the as-produced Mn_{12}–ac.

Chemical Characterization

The films were characterized as to their chemical makeup using X-Ray Photoelectron Spectroscopy (XPS). XPS is a technique in which a sample is bombarded by x-rays of a known energy. The x-rays probe the first few surface layers of the sample, ejecting outer shell electrons from the atoms making up the sample. These electrons are collected and their kinetic energies measured. The difference between the kinetic energy of the ejected photoelectron and the energy of the incident x-rays is the binding energy of the electron when it was still in the sample. This binding energy is highly dependent on the binding state of the atom from which it was ejected. This technique, then, allows for precise characterization of the chemical makeup of the surface being measured. Not only the types of atoms, but also their binding states, can be well determined. Characteristic peaks for atoms in many different configurations are well documented [67]. Comparison of the integrated area under peaks corresponding to different electron orbitals can be compared to determined the stoichiometric makeup of the material.

Films created with the two sets of criteria mentioned above, as well as the as-produced Mn_{12}–ac were measured using XPS. The peaks for Mn 2p, O 1s, and C 1s electrons are shown in figures 9, 10, and 11, respectively. The data were normalized to unity at the

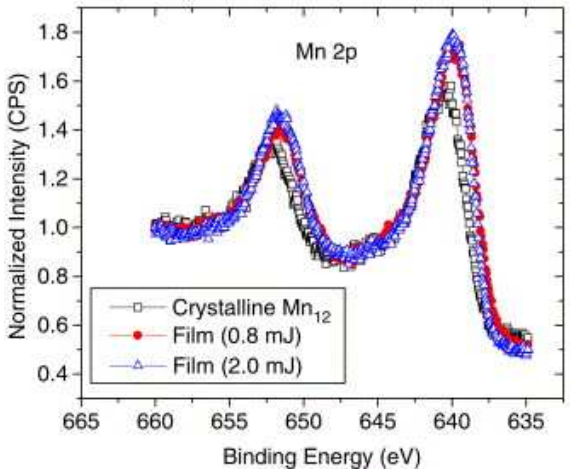

Figure 9: Binding energy spectrum for Mn 2p orbitals. Curves for the as-produced Mn_{12}–ac and films produced with the nitrogen laser with two different sets of deposition criteria (8 Hz at 0.8 mJ and 20 Hz at 2.0 mJ) are shown here, normalized to unity at the highest binding energy. Reprinted with permission from [33], Copyright 2004 by Elsevier B.V. (doi:10.1016/j.jmmm.2004.06.057).

highest binding energy to aid in comparisons. In figure 9 it can be seen that the peak positions for the electrons from the Mn 2p orbitals have changed very little in the ablated films relative to those of the starting material. The two peaks, at 652.0 eV and 640.2 eV, correspond to the $2p^{1/2}$ and $2p^{3/2}$ orbitals, respectively. The values found here for the as-produced Mn_{12}–ac are in good agreement with those found by Kang, et al. [68], using photo-emission spectroscopy.

Di Castro and Polzonetti [69] have studied changes in binding energy for the Mn $2p^{1/2}$ electrons as manganese is oxidized to form various manganese oxides. The binding energies found for the Mn atoms in Mn, MnO, Mn_3O_4, Mn_2O_3, and MnO_2, respectively, were found to be 639.2 eV, 641.0 eV, 641.5 eV, 641.9 eV, and 642.6 eV, each with an error of ± 0.2 eV. In the present experiment, shifts in the binding energy in the ablated material relative to that of the starting material are on the order of 0.5 to 0.7 eV. Taken in light of the findings of Di Castro and Polzonetti, there is indication that these shifts could be due to changes in the binding state of the Mn atoms in the material. As will be

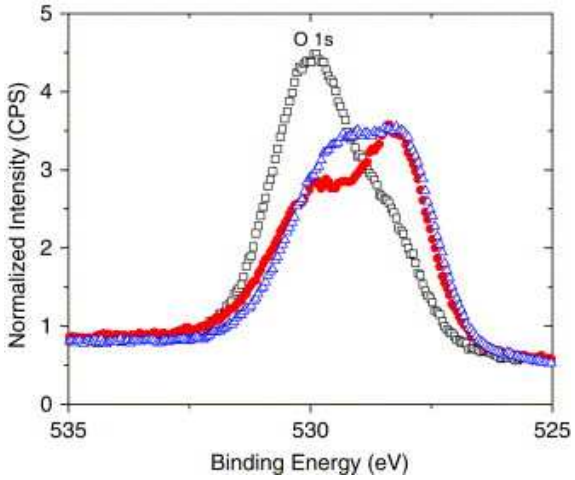

Figure 10: Binding energy spectrum for O 1s orbitals. Curves for the as-produced Mn_{12}–ac and films produced with the nitrogen laser with two different sets of deposition criteria (8 Hz at 0.8 mJ and 20 Hz at 2.0 mJ) are shown here, normalized to unity at the highest binding energy. See figure 9 for legend. Reprinted with permission from [33], Copyright 2004 by Elsevier B.V. (doi:10.1016/j.jmmm.2004.06.057).

discussed later, these shifts are in agreement with changes in the magnetic properties of the molecules. Based on these XPS data, it is not possible to rule out the presence of any of these manganese oxides, since their peak could be hidden within the two known peaks for Mn_{12}–ac.

The binding energy of the O 1s orbital electrons, as seen in figure 10, shows two peaks, with the smaller peak appearing as a shoulder on the lower-energy side of the larger peak. The peak at 528.1 eV (the shoulder) corresponds to the oxygen atoms in the core of the Mn_{12}–ac molecules, while the peak at 529.9 eV corresponds to the oxygen atoms in the acetate ligands and water molecules surrounding the core. These values are also in agreement with those found by Kang, et al. [68]. Small shifts from the published values may be attributed to charging effects due to the insulating nature of the silicon substrate used. The ablated material shows no significant shift in the peak positions relative to those of the starting material, but the relative intensities of the two peaks show an appreciable change. The higher energy peak (oxygen in water and acetate ligands) shows a marked

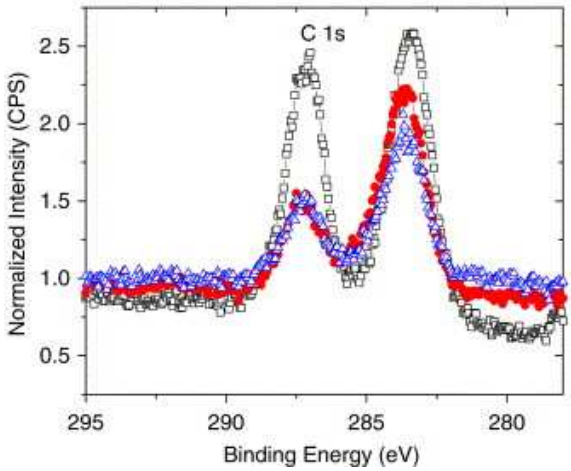

Figure 11: Binding energy spectrum for C 1s orbitals. Curves for the as-produced Mn_{12}–ac and films produced with the nitrogen laser with two different sets of deposition criteria (8 Hz at 0.8 mJ and 20 Hz at 2.0 mJ) are shown here, normalized to unity at the highest binding energy. See figure 9 for legend. Reprinted with permission from [33], Copyright 2004 by Elsevier B.V. (doi:10.1016/j.jmmm.2004.06.057).

decrease in intensity in the ablated material relative to that of the starting material. The integrated intensity of the peak for the oxygen atoms in the magnetic core, however, shows little change. This is consistent with the removal of surrounding ligands with little change to the Mn core.

Figure 11 shows the binding energy spectrum for the C 1s orbital electrons. This spectrum also shows two peaks; one at 283.3 eV and one at 287.1 eV, corresponding to carbon atoms in two different bonding states within the acetate ligands. Neither peak shows an appreciable change in position, but both show significant reduction in intensity. Again, this is consistent with the removal of acetate ligands during the ablation process.

When taken all together, the XPS data seem to indicate that the core of the Mn_{12}–ac molecules remains intact while some of the surrounding water and acetate ligands are lost. Since magnetic features of the molecule are a result of interactions within the core, we would expect to see magnetic features in the films similar to those seen in as-produced Mn_{12}–ac. However, the removal of acetate and water ligands from the outside of the

molecules could lead to enhanced interactions between neighboring molecules. Features consistent with this are seen in the magnetic data that follows. It should also be noted that an attempt was made to use mass spectrometry to confirm the chemical makeup of the ablated material, but the small amount of material in the films made with the nitrogen laser led to inconclusive measurements of the mass spectrum. In earlier work done using a laser ablation technique with a KrF excimer laser [35], mass spectrometry data showed that when lowering the pulse rate used in the ablation, and therefore the total power put into the material, the fragmentation of the Mn_{12}–ac was reduced to minimal levels. Use of the nitrogen laser allowed for much lower pulse energies (0.8 - 2.0 mJ compared to 200 - 450 mJ) with higher repetition rates (8.0 - 20 Hz compared to 1 - 3 Hz), yielding lower overall power. It follows that the fragmentation of the Mn_{12}–ac would be even less in the nitrogen laser ablated films than that seen in the lowest power excimer laser ablated films.

Magnetic Characterization

Magnetic characterization of the ablated material was carried out with a Quantum Design MPMS SQUID Magnetometer. Due to the small amount of material in the ablated films and the large diamagnetic background signal of the silicon substrate, it was not possible to perform the magnetic measurements on the films themselves. Instead the ablated Mn_{12}–ac was scraped from the substrates and measured in powdered form. The material used for the following measurements was from the film created with a pulse rate of 8 Hz and an energy of 0.8 mJ.

As discussed in chapter II, magnetization data taken on the starting material show a strong hysteresis at temperatures below T_B, due to the "blocking" of the magnetic state of the molecules. There are also steps seen on the sides of the curve where $|H|$ is increasing due to quantum tunneling of the magnetization. Figure 12 shows the magnetization, M, of

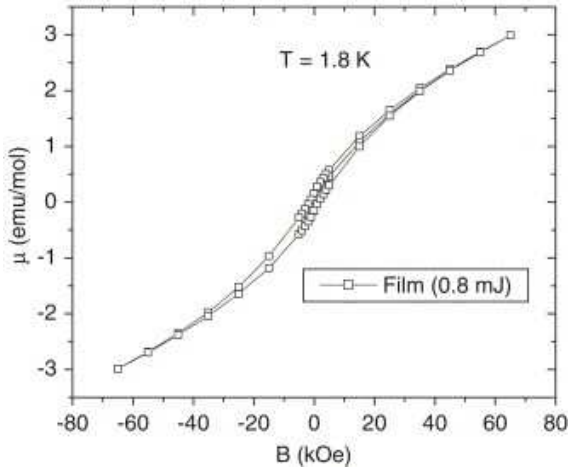

Figure 12: Magnetization of ablated material as a function of applied field at 1.8 K. Narrowed hysteresis (as compared to the starting material) and a lack of steps are notable features. Reprinted with permission from [33], Copyright 2004 by Elsevier B.V. (doi:10.1016/j.jmmm.2004.06.057).

the ablated material as a function of the applied field, H, at 1.8 K. Here it should be noted that hysteresis is still seen, although the width of the hysteresis loop is greatly narrowed compared to that of the starting material. It is also notable that the characteristic steps in the hysteresis loop are not seen. These observations may both be due to the random orientation of the Mn_{12}–ac molecules in the material. Larger crystals in the starting material lead to enhancement of these features. However, the presence of hysteresis at all indicates that there is still a superparamagnetic blocking of the magnetization at low temperature.

The magnetic moment of the ablated material as a function of temperature is shown in figure 13. The sample was cooled in zero field and measured in a field of 50 Oe on warm-up. The sample was then cooled again in a field of 50 Oe and measured in the same field on warm-up. The blocking temperature, T_B, is usually specified as the point where the field-cooled and zero-field-cooled curves split. In a crystalline Mn_{12}–ac sample, this is also where the zero-field-cooled curve reaches a local maximum, at $\sim$3 K. In the curves seen in figure 13, however, the splitting of the curves happens at $\sim$45 K. The curve also shows two local maxima, the typical one seen at low temperature and another which appears at

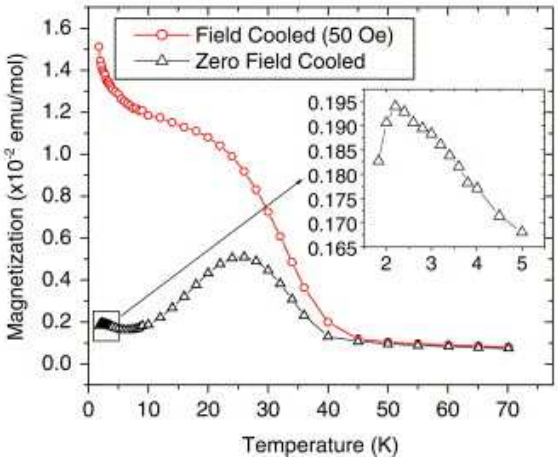

Figure 13: Magnetic moment of ablated material as a function of temperature in a field of 50 Oe. Curves for material cooled in zero field and in a field of 50 Oe were measured. The inset shows the zero-field-cooled data in the temperature range from 1.8 to 5 K. Reprinted with permission from [33], Copyright 2004 by Elsevier B.V. (doi:10.1016/j.jmmm.2004.06.057).

$\sim$27 K. The lower temperature maximum is shifted down to 2.2 K, indicating a lowering of the blocking temperature for the magnetic phase which is dominant in the crystalline Mn_{12}–ac. The presence of the higher temperature maximum seems to indicate the presence of another magnetic phase within the ablated material. This additional phase could be due to clusters of interacting molecules. The enhanced interaction is consistent with the removal of acetate ligands which was indicated by the XPS data. Removal of the outer ligands allows the molecules to be closer together, allowing for enhanced interactions. The additional peak could also be due to fragmentation of the Mn_{12}–ac molecules. The higher temperature magnetization is consistent with that seen in nanoclusters of MnO [70, 71].

Overall, we have shown that laser ablation is a simple, yet viable, process for making thin films of Mn_{12}–ac. The important magnetic feature of superparamagnetic blocking at low temperature is still exhibited. Formation of an additional feature in the magnetization data is an interesting result which should be explored further.

Drop-and-Dry

Another, even simpler, method for creating thin films up to a few monolayers of Mn_{12}–ac was developed by other students in the lab [36, 37]. This method, known as the dip-and-dry (DAD) method, consists of dissolving Mn_{12}–ac powder in a solvent, dipping a substrate into the solvent, and allowing the solvent to evaporate, leaving behind the Mn_{12}–ac molecules. A closely related drop-and-dry method, in which the solution is dropped onto the substrate, can also be used.

The dip-and-dry (or drop-and-dry) method has the advantage of creating high-quality films of Mn_{12}–ac, but it cannot be used for making films of more than a few nanometers in thickness. The pulsed laser deposition technique allows for creation of very thick films, with time and patience being the main constraints. However, the quality of the films created by laser ablation is still in question. Because the present research only concerns surface layer interactions, a thin film (even a single monolayer) will suffice, so the drop-and-dry method is used for the electronic measurements detailed in chapter VI.

CHAPTER V

DILUTION REFRIGERATOR THEORY AND OPERATION

Theory

Much has been written on the operation of dilution refrigerators. Here I give only a brief description and will refer the interested reader to books by Lounasmaa [72] and Pobell [73] for an in-depth explanation of the physics behind a dilution refrigerator. One physical principal, which is a unique property of a mixture of ^{3}He and ^{4}He, allows for the functioning of a dilution refrigerator. For a mixture of ^{3}He and ^{4}He, below $\sim$700 mK, with a concentration >6% ^{3}He, the mixture separates into two phases: a ^{3}He-rich phase and a ^{3}He-dilute phase. The unique property that allows the dilution refrigerator to function is that the ^{3}He-dilute phase cannot go below 6% ^{3}He, even at zero Kelvin. This property is exploited by pumping on the ^{3}He-dilute phase, thereby removing ^{3}He from the system. Because the dilute phase cannot have less than 6% ^{3}He, ^{3}He atoms are forced to diffuse, or evaporate, across the phase boundary. This evaporation requires energy to account for the latent heat of evaporation. The energy comes from the surrounding system, causing the temperature to be lowered. Direct thermal contact between the mixing chamber (where the phase boundary exists) and the sample allows the sample to be cooled. This is the basic operating principle. In practice, the system required to successfully exploit this phenomenon is quite complex.

Components

Figure 14 shows a diagram of the working components of a dilution refrigerator. As noted above, the phase separation surface occurs in the mixing chamber, making it the coldest point in the refrigerator. Due to the heavier mass of ^{4}He, the ^{3}He-dilute phase is below

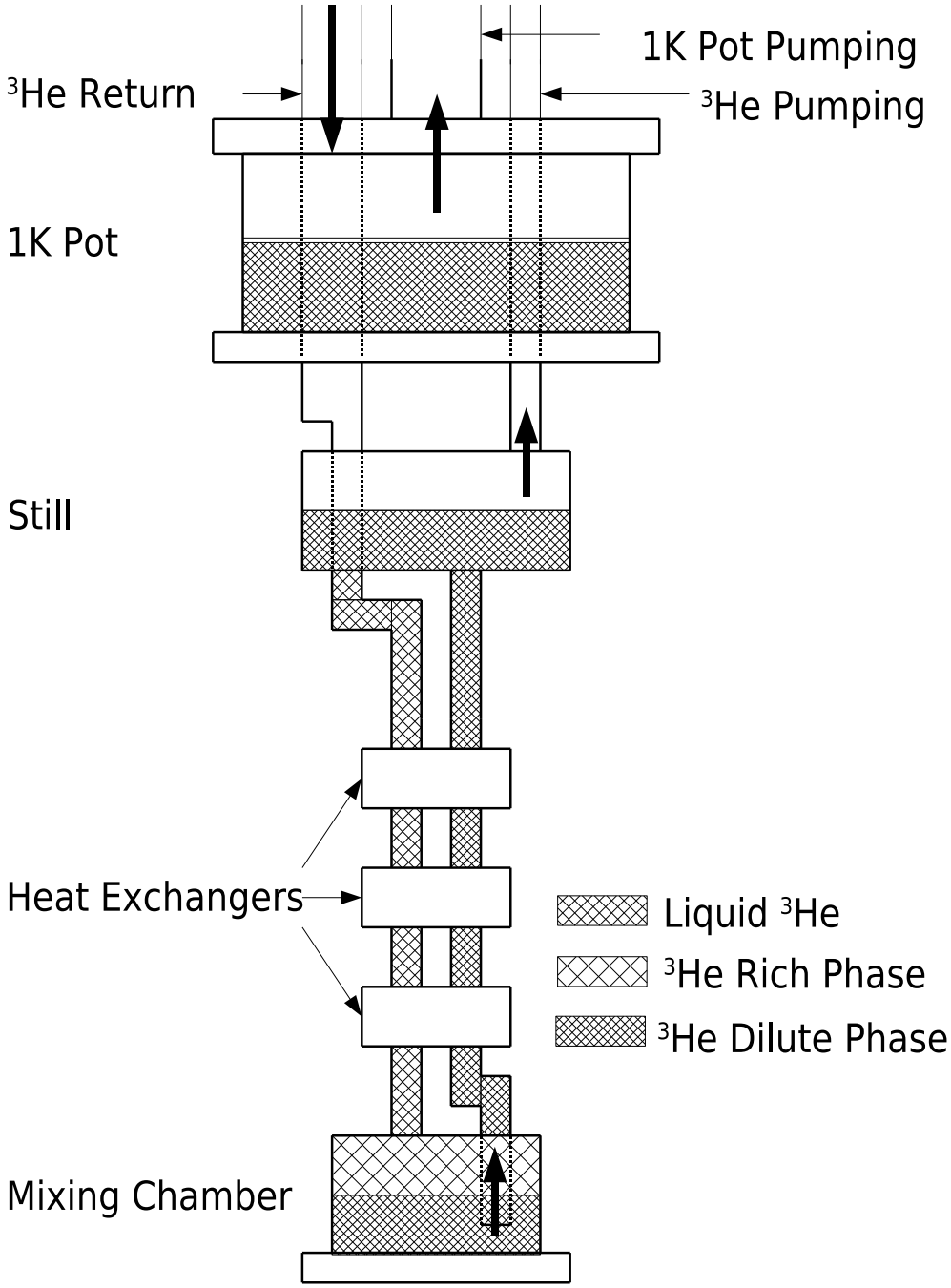

Figure 14: Schematic of dilution refrigerator. Note that the bold arrows indicate flow direction.

the ^{3}He-rich phase. The mixing chamber is connected to the still by a capillary. Note that the capillary goes to the bottom of the mixing chamber so that the liquid in the still is from the ^{3}He-dilute phase. A closed-cycle circulation pump is used to pump on the still. Because the vapor pressure of ^{3}He is higher than that of ^{4}He at low temperatures, the vast majority of what is pumped out is ^{3}He. The ^{3}He gas which is removed is returned to the ^{3}He-rich side via the ^{3}He Return Line noted in the figure. The 1 Kelvin Pot (or 1 K Pot) is a simple bath of ^{4}He which is pumped on to lower the temperature to $\sim$1 K. This reservoir serves to condense the ^{3}He which is returned to the system. The condensed mixture then is passed through the still (which is maintained by means of heating at about 700 mK) to further cool it. The returned ^{3}He, as well as the ^{3}He which is being transferred from the mixing chamber to the still, is passed through a series of heat exchangers which serve a dual purpose. They help to cool the returned ^{3}He even further while helping to warm the outgoing ^{3}He in order to help with its ability to be pumped away. As mentioned earlier, the still is heated to maintain a temperature of $\sim$700 mK. This is crucial to the operation of the dilution refrigerator. While it may seem counter-intuitive that one must add heat in order to cool the system, the explanation is simple. Since the cooling power of the system depends on the amount of ^{3}He which is evaporating across the phase boundary, the more circulation there is, the more cooling power there will be. Therefore, one must heat the still in order to add the necessary energy that allows the ^{3}He to evaporate more easily and be pumped away, increasing the circulation rate.

During operation, the system is sealed inside a vacuum can. The entire system is immersed in a bath of liquid ^{4}He, which has a temperature of 4.2 K. A major obstacle in effective cooling of a dilution refrigerator can be heat leaks from external sources. Each of the major parts shown in figure 14 (1 K Pot, Still and Mixing Chamber) are on individual stages. These stages consist of a copper platform separated from the other stages by graphite rods. Graphite is a poor thermal conductor and serves to thermally isolate each

stage from the others. In order to prevent radiant heating of the sample space from the 4.2 K surfaces of the vacuum can, there is a fiberglass radiation shield between the vacuum can and the system. This shield is attached to the stage containing the 1 K pot, so it is nominally at a temperature of 1 K. Another measure that must be taken is to ensure that all wiring and capillaries must be well coupled thermally to each stage as they pass down from the top of the system.

The actual operation of the dilution refrigerator requires quite a number of peripheral systems. A significant amount of time and effort was devoted to determining the layout of the plumbing for the gas-handling system on this system. As mentioned, a sealed circulation pump (an oil-based mechanical pump) is required to pump out the ^{3}He and return it. There is also a diffusion pump which can be used for circulation. The diffusion pump is backed by the sealed circulation pump. Storage tanks are required for the mixture when it is in gas form. Another diffusion pump, with an associated mechanical backing pump, is used for evacuating the vacuum can before cool-down. This diffusion pump can also be used for pumping out the circulation system once the majority of the mixture has been removed from circulation to ensure that there are no plugs of solidified nitrogen, oxygen or air in the capillaries. An additional mechanical pump is used for pumping on the 1 K pot. These pumps are vented to atmosphere.

Pressure measurement is a crucial aspect of operating the dilution refrigerator. As such, our system employs several TC gauges for measurement of rough vacuum in different places, including the pumping side of the circulation path. A Bayer-Alpert type ionization gauge is used for measuring the high vacuum in the vacuum can. The pressure on the return side of the circulation path (which can range from 1 Torr to atmospheric pressure [760 Torr]) is measured with a diaphragm gauge. All of these pressure gauges are read with digital gauge controllers. Pressure in the 1 K pot is measured with a high-precision Wallace and Tiernan analog dial gauge.

In addition to all of these working components, there is also substantial electrical wiring involved. This wiring is used for thermometry and sample measurement. See appendix A for information on wiring for this particular dilution refrigerator.

Operation

Following is a description of the general cool-down procedure. After all electrical connections are made for the samples, the radiation shield is put into place. The vacuum can is then put into place and sealed with an indium seal. After rechecking all electrical connections, the vacuum can is evacuated to a vacuum of $\sim 10^{-5}$ Torr. While the vacuum can is being pumped out, some peripherals are attached to the system. The superconducting magnet is hung and its leads are attached. Superconducting level meters (to determine the liquid level of the helium bath) are attached and tested. An extension for the liquid helium fill line, which reaches to the bottom of the liquid helium dewar, is attached. Lastly, the dewar for the liquid helium bath is raised and bolted into place. After the vacuum can is sufficiently evacuated, it is back-filled with a small amount ($\sim$1000 mT) of ^{3}He exchange gas. This serves the purpose of providing a thermal link between the parts of the dilution refrigerator which are inside the vacuum can (which are nominally thermally isolated from the vacuum can itself during operation) and the vacuum can. The system can then be pre-cooled with liquid nitrogen. This consists of pumping out the dewar (to ensure there are no large pieces of ice forming inside the dewar) and back-filling it with nitrogen gas then filling the dewar with liquid nitrogen. This will bring the temperature of all parts of the system to 77 K.

After the temperature of the system is stable at 77 K, the remaining liquid is pushed back out of the dewar (this is part of the reason for adding the extension mentioned earlier, which reaches to the bottom of the dewar). The dewar is then pumped out again and back-

filled with helium gas. The reason for this is to make sure that no significant amount of nitrogen remains in the dewar. Any nitrogen which remained during the liquid helium transfer would be solidified and act as a large heat sink, boiling off significant amounts of liquid helium. Liquid helium is then transferred from an external storage dewar into the experimental dewar. Transfer is made using a flexible, vacuum insulated, transfer line, made by Cryo Industries. Transfer progress is monitored using thermometers within the cryostat as well as superconducting level meters mounted on the outside of the cryostat, within the dewar. After the liquid helium transfer, the components inside the vacuum can should be at 4.2 K. After ensuring that this is the case, the vacuum can is pumped with a diffusion pump to remove the ^{3}He exchange gas. Once the pressure inside the vacuum can is down to $\sim 5 \times 10^{-6}$Torr, the vacuum can is isolated from the external systems by closing a valve. This concludes the pre-cooling procedure.

The final cooling of the dilution refrigerator begins by starting the 1K pot. The pot is pumped out by a large mechanical pump. After it is pumped down to hard vacuum, it is filled with liquid helium. The filling is done through a tube which extends into the liquid helium bath of the dewar and is connected to the 1K pot through a needle valve. The valve is opened, allowing liquid helium to flow into the pot. This causes the pressure within the pot to rise. Once the top surface of the liquid moves from the fill tube into the pot itself, the pressure levels off as the pot continues to fill. Once the pot is full, the liquid level moves into the pumping line above the pot. This causes the pressure to begin rising again. This is a simple way to detect when the pot is full. At this point, the needle valve is closed. Within a few minutes, the pressure in the 1K pot is down to base pressure and the temperature is $\sim$800 mK.

Once the 1K pot is operating, the ^{3}He–^{4}He mixture can be added to the system. The mixture is added on the pumping side of the circulation system. This is because the pumping side has much larger tubing in the low temperature parts of the system than the return

side, allowing any impurities in the mixture to be frozen out in a large diameter pipe, helping reduce the likelihood of forming a plug in a capillary within the circulation system. After the mixture is added, time is allowed for the mixture to condense into the system. The 1K pot serves to condense the mixture, which can then flow into lower parts of the circulation system. After the pressure on the pumping side has leveled off (indicating maximum condensation), circulation can be started. An essential part of the circulation system is a liquid nitrogen cold trap, which must be cooled before circulation is started. This helps freeze out any impurities in the mixture outside of the cryostat, including possible oil vapor from the circulation pump itself. Once circulation begins, the cryostat cools very quickly. Nominally, the base temperature can be reached within a couple of hours.

Thermometry

A critical aspect of any low temperature work is the ability to measure temperature. Thermometry at low temperatures can be achieved in a number of ways (for a brief discussion of several techniques, see [74]). The thermometry in our system is handled using several resistive thermal devices (RTD's). Diagnostic thermometry (used to help determine proper operation of the system) is handled by several carbon resistors. The exact type of resistors used could not be determined from the documentation available, but calibration curves for these thermometers were found. Carbon resistors are located in the 1K pot, the still and the mixing chamber as well as four of the heat exchangers. These thermometers are measured with a 2-wire AC lock-in technique. The temperature is determined by comparing the measured resistances with the available calibration curves. The values are offset from those in the available data, and the 4.2K value is used to determine the offset. The offset is assumed to be a constant value, independent of temperature. Since these thermometers are only used for diagnostic purposes, the precision is not crucial.

There are also two other matched (approximately) carbon resistors used for diagnostic purposes during cool down. One is mounted outside of the vacuum can, in the helium bath, and the other is inside the vacuum can, on the mixing chamber stage. These two resistors are monitored using a digital multimeter. Keeping the values of these two thermometers close during cool down helps ensure that the inside of the vacuum can is cooling as the outside cools.

The temperature of the sample is determined by measuring a ruthenium oxide (ROx) resistor produced by Lake Shore Cryotronics (model #RX-202A, serial #U01955). This thermometer is mounted on the stage containing the mixing chamber. Good thermal contact between the mixing chamber and the sample stage should ensure that they are at the same temperature. Model RX-202A ROx resistors from Lake Shore follow a standard resistance vs. temperature curve with an accuracy of $\pm$ 250 mK at 4.2 K and $\pm$15 mK at 50 mK (shown in Appendix H. The standard curve gives values in the temperature range from 0.050 to 40.0 K. Since our particular ruthenium oxide sensor was uncalibrated, the standard curve was used for all measurements of the sample temperature. Measured values for our particular resistor are given for room temperature, liquid nitrogen and liquid helium. Measurement of the ROx thermometer is done with a 4-wire AC lock-in technique.

For comparison, a germanium resistor, also from Lake Shore Cryotronics (model #GR-200A-100, serial #21271), is also mounted on the mixing chamber stage. This particular resistor was calibrated by Lake Shore in the temperature range from 0.257 to 7.16 K. A spline fit to the data using Chebychev polynomials in two temperature ranges was used to create an interpolation table of resistance vs. temperature data in the temperature range from 0.3 to 6 K. This resistor was also measured using a 4-wire AC lock-in technique. Calculated temperatures using the ROx and Ge resistors were generally in good agreement.

CHAPTER VI

EXPERIMENTAL PROCEDURES AND RESULTS

Sample Preparation

For measurement of the resistance of gold with and without Mn_{12}–ac, gold was deposited onto a silicon substrate in the pattern shown in figure 15. This pattern consists of a single current-carrying strip with eight voltage probes. Both ends of the current-carrying strip and each of the probes have large contact pads for ease of mounting the samples. By placing Mn_{12}–ac on half of the current-carrying strip, this design allows for simultaneous four-wire measurements of the resistance of the gold with and without Mn_{12}–ac.

The silicon substrate was cleaned by sonication in acetone followed by a rinse with clean acetone and a rinse with clean isopropyl alcohol. The substrate was then mounted behind a shadow mask in an evaporation chamber. The evaporation chamber was evacuated to a pressure of $4 - 6\times10^{-6}$ Torr by means of a diffusion pump. A 20 Å layer of germanium was evaporated onto the substrate followed by a layer of gold. The thicknesses

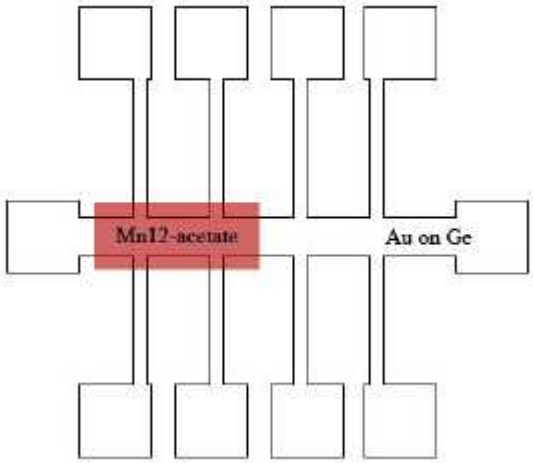

Figure 15: Pattern used for resistance measurements.

of the gold films varied between samples and will be specified in the section on data and results later in this chapter. Film thicknesses were measured using a calibrated quartz crystal microbalance (QCM). The gold used for the samples was 99.99% pure with 5 ppm Cu, 22 ppm Ag, and 4 ppm Fe (based on spectrometric analysis by atomic absorption performed by the manufacturer). The germanium layer served as an adhesion layer, as gold does not adhere well to silicon.

As mentioned in chapter IV, the drop-and-dry method was used to deposit Mn_{12}–ac on the surface of the gold. A solution was prepared by dissolving 1 mg of powdered Mn_{12}–ac in 10 ml of isopropyl alcohol. The solution was sonicated in an ultrasonic bath to aid in full dissolution of the Mn_{12}–ac. After the solution was allowed to sit for a few minutes so that any undissolved Mn_{12}–ac settles out, the solution was drawn into a hypodermic needle for deposition on half of the main current-carrying path of the gold film. One drop of the solution was dropped at a time onto the desired substrate and the isopropyl alcohol was allowed to evaporate between drops. It has been shown that, with the given concentration, the first drop deposits about one smooth molecular layer [36]. Subsequent drops tend to lead to clustering of the Mn_{12}–ac on the surface. Using a lower concentration of Mn_{12}–ac can lead to a more sparse coverage, while a higher concentration doesn't allow for full dissolution of the molecules into the isopropanol, leaving large clusters in suspension. Magnetic studies have shown that the Mn_{12}–ac maintains its interesting magnetic properties after short exposure to isopropyl alcohol. Samples used in this study were made using the drop-and-dry method with five drops unless otherwise noted.

After fabrication, the samples were prepared for mounting in the dilution refrigerator. The dilution refrigerator is equipped with 16-pin DIP sockets to which the sample measurement leads are attached. Samples are mounted onto an "L"-shaped part (L-bridge) made of oxygen-free high conductivity (OFHC) copper. The L-bridge allows for the sample to be put into good thermal contact with the cold finger of the dilution refrigerator,

instead of being mounted directly to the plastic DIP socket. A sample was adhered to the L-bridge with GE Varnish (General Electric product number 7031). GE varnish has a good thermal conductivity with very poor electrical conductivity and is quite resilient to thermal cycling. Gold wires were used to make electrical connections from the sample to a 16-pin DIP header which was attached to the L-bridge. The wires were soldered to the DIP header. Contact on the sample was made by pressing indium onto the contact pads, pressing the gold wire into the indium, and then pressing another piece of indium on top of the gold wire. The DIP header was inserted into the DIP socket on the cold finger of the dilution refrigerator and a screw was used to bring the L-bridge into good thermal contact with the cold finger.

Measurement Procedures

Resistance measurements were carried out using a standard four-wire ac lock-in technique. Two Princeton Applied Research (PAR) model 124A lock-ins were used in a master-slave configuration. Unless otherwise noted, the measurement procedures were the same for all samples. An output voltage of 1.0 V was generated by the master lock-in at a frequency of 23 Hz. The supplied current was split to go to the sample and into the external reference input of the slave lock-in. The slave used the frequency from the master as a reference for locking onto the ac signal on its inputs. The 1.0 V reference signal was sent through a 100 kΩ resistor to the sample, resulting in a current of 10 μA. The voltage drop for a section of the current-carrying path with or without Mn_{12}–ac was measured by attaching the voltage leads to a PAR model 113 voltage pre-amplifier. The PAR 113 was set to filter the signal using low-pass and high-pass filters set to 0.1Hz and 1.0 kHz, respectively. A gain of 10–500 was selected to get the largest signal that the PAR 124A could read without overloading. The output from the PAR 113 pre-amp was sent into a PAR model 116 pre-

amplifier in the PAR 124A lock-in amplifier set to Direct mode (100 MΩ, 30 pF input). At the beginning of each measurement, after the temperature was stabilized and before the magnet was energized, the phase of the signal was adjusted so that the out-of-phase component was minimized. The sensitivity was set to 500 mV and the time constant was set to either 3 sec. or 10 sec. The signal monitor output of the lock-in was connected to the interface panel for the Keithley 2700/7700 multimeter/scanner described in appendix A. An identical setup was used with the slave lock-in, measuring another part of the given sample.

The magnetic field was supplied by a superconducting magnet, from Cryogenic Consultants Limited, rated at > 13.0 T at 4.2 K. The charging of the magnet was controlled by a home-built controller and current up to 120 A was supplied by a pair of Hewlett Packard model 6260B DC Power Supplies in a master-slave configuration. The magnet current was measured by measuring the voltage across a shunt resistor which was placed in-line with the main current leads to the magnet. The magnetic field was then calculated using the manufacturer-supplied rating of 0.1228 Tesla/Amp.

In order to take the desired resistance measurements, the current limit was stepped to the desired value on the magnet power supply controller and the magnet was charged. After waiting an appropriate amount of time for the lock-in to stabilize (generally >10 time constants) the values of the voltages for both parts of the sample (with and without Mn_{12}–ac) were recorded, along with the current in the magnet.

Experimental Data and Conclusions

Measurements were made for comparison on samples of varying thicknesses. The samples were also measured at various temperatures to try to find temperature-dependent trends.

Representative data from selected samples are shown here and the general trends are discussed.

Figure 16 shows the change in resistance, with respect to the applied magnetic field, of a 7.8 nm gold film with and without Mn_{12}–ac, measured at 600 mK. The filled points are the experimental data, while the solid lines are fits to the data using equation 13. Fits were achieved with a least-squares fit, as outlined in appendix C. While the data are noisy, the theoretical fits are reasonable and the values obtained from the fit for the pure gold are in line with previously published results [56]. The characteristic fields and corresponding scattering times for these curves, along with the associated errors, are tabulated in table 1. Referring to table 1, the change in scattering times for the two parts of the sample indicate that there is reduced elastic scattering (more time between events). This is consistent with a change in the surface morphology of the system. Surface scattering events are elastic. Changing the surface can lead to a reduction in elastic scattering. The spin-orbit scattering and inelastic scattering are essentially unchanged. The main feature to note is the significant decrease in the spin scattering times. This indicates addition of a significant source of spin scattering.

Figure 17 shows the change in resistance for a 9.0 nm gold film with and without Mn_{12}–ac, again measured at 600 mK. Characteristic scattering times and fields for the 9.0 nm sample are listed in table 2. As with the 7.8 nm sample, the elastic scattering times are increased in the presence of Mn_{12}–ac, indicating a decrease in the frequency of elastic scattering events, while the spin-orbit scattering time remains unchanged. Within the experimental error for the inelastic scattering time, there is no appreciable change.

The most notable feature, again, is the significant increase in spin scattering frequency relative to that seen in the pure gold film.

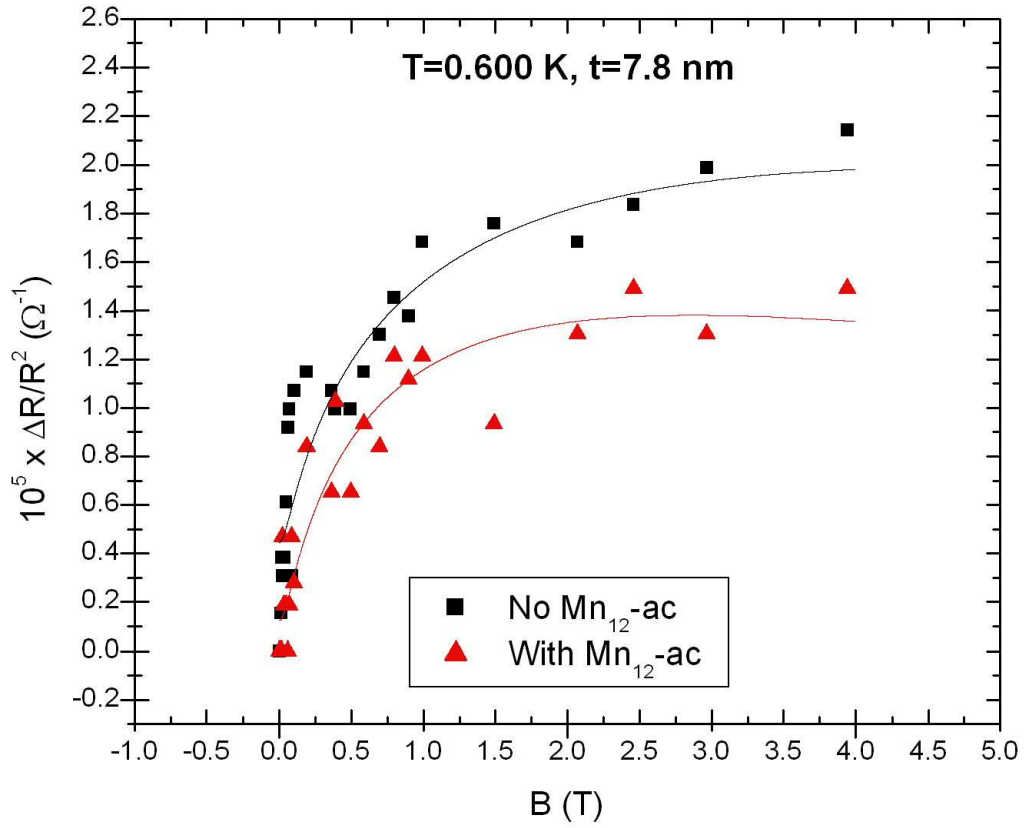

Figure 16: Magnetoresistance of 7.8 nm Au film at 600 mK. Solid curves are fits to theory.

Table 1: Characteristic fields and scattering times for 7.8 nm gold film at 600 mK.

	No Mn_{12}–ac	With Mn_{12}–ac
H_0	12.9±0.5	4.3±0.2
H_i	0.0145±0.005	0.0090±0.0045
H_{so}	0.97±0.02	0.58±0.02
H_s	0.0040±0.0025	0.0080±0.0020
τ_0	$(3.62\pm0.07)\times10^{-15}$	$(6.31\pm0.15)\times10^{-15}$
τ_i	$(3.66\pm1.20)\times10^{-12}$	$(3.97\pm1.92)\times10^{-12}$
τ_{so}	$(4.85\pm0.01)\times10^{-14}$	$(4.76\pm0.05)\times10^{-14}$
τ_s	$(1.91\pm1.17)\times10^{-11}$	$(3.59\pm0.82)\times10^{-12}$

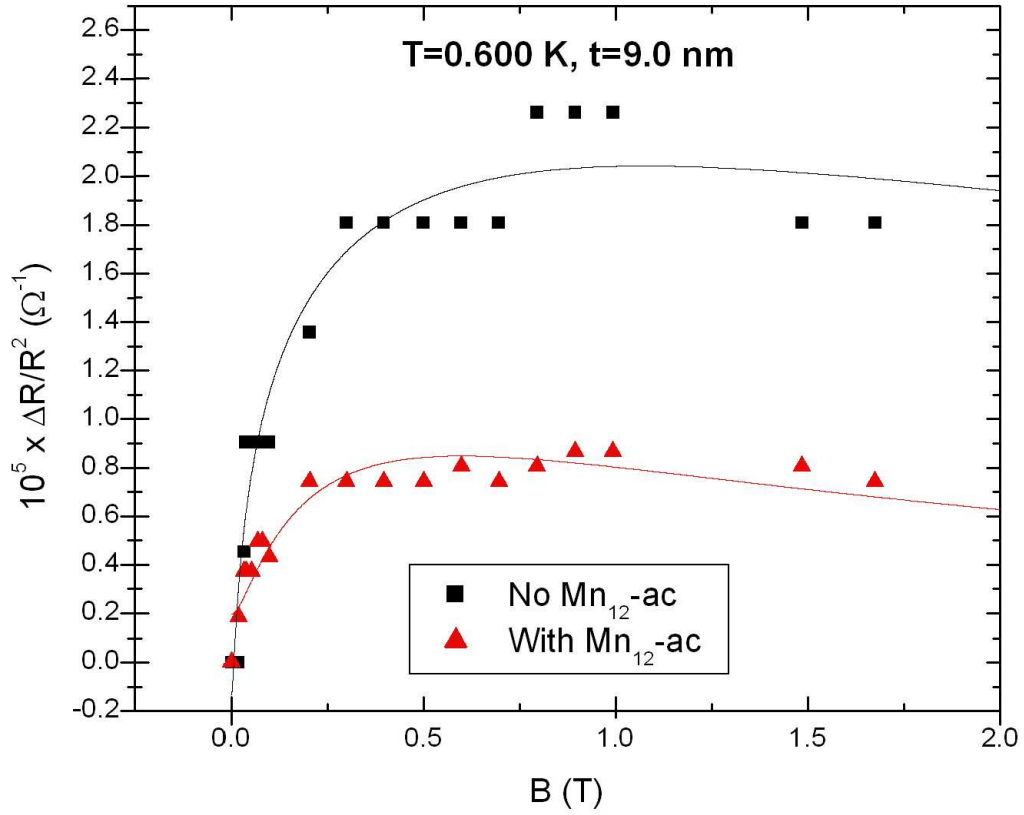

Figure 17: Magnetoresistance of 9.0 nm Au film at 600 mK. Solid curves are fits to theory.

Table 2: Characteristic fields and scattering times for 9.0 nm gold film at 600 mK.

	No Mn_{12}–ac	With Mn_{12}–ac
H_0	3.1±0.4	0.5±0.1
H_i	0.0015±0.001	0.0050±0.0045
H_{so}	0.23±0.02	0.12±0.02
H_s	0.0005±0.0004	0.0050±0.0030
τ_0	$(7.47\pm0.48)\times10^{-15}$	$(1.88\pm0.18)\times10^{-15}$
τ_i	$(2.63\pm1.66)\times10^{-11}$	$(8.78\pm7.72)\times10^{-12}$
τ_{so}	$(9.99\pm0.21)\times10^{-14}$	$(7.75\pm0.51)\times10^{-14}$
τ_s	$(4.60\pm2.16)\times10^{-11}$	$(2.70\pm1.43)\times10^{-12}$

Figure 18 shows the change in conductance of the same 9.0 nm gold film shown in figure 17, with and without Mn_{12}–ac, but measured at 54 mK. Table 3 lists the characteristic fields and scattering times for the fits shown.

At this lower temperature, there is still an appreciable increase in the elastic scattering time in the presence of Mn_{12}–ac. There is also still substantial increase in the spin scattering time. It should be noted, however, that there is now a significant decrease in the inelastic scattering time and a significant decrease in the spin-orbit scattering time. The reason for this change is unknown.

The magnetoresistance of the 9.0 nm gold film was also measured in a magnetic field parallel to the film plane. Figure 19 shows the magnetoresistance data acquired. An attempt was made to fit this data with weak localization theory (equation 18). However, as pointed out by Giordano and Pennington [56], even small errors in the alignment of the magnetic field relative to the plane of the film can give a considerable contribution to the perpendicular magnetoresistance. The sample-mounting stage of our dilution refrigerator has one sample mount parallel to the magnetic field, but it is only roughly parallel (within a few degrees). Without a second magnet to "shim" the field direction or a rotational stage to get better alignment, it is not possible to do an adequate measurement of the magnetoresistance in parallel field.

In figure 20, the change in resistance of the 9.0 nm gold film is plotted as a function of temperature in zero magnetic field. This data was acquired using Labview taking one data point per second as the temperature was swept up. The temperature sweep was achieved by adding heat to the mixing chamber heater on the dilution refrigerator. Since this was manually controlled, the sweep rate was not constant in general. Because of the large amount of data, every two minutes of data (or, 120 data points) was averaged together to obtain the points for the plot. Due to these factors, there is no data in the 3 K range of temperature. This would be of interest because it corresponds to the blocking temperature

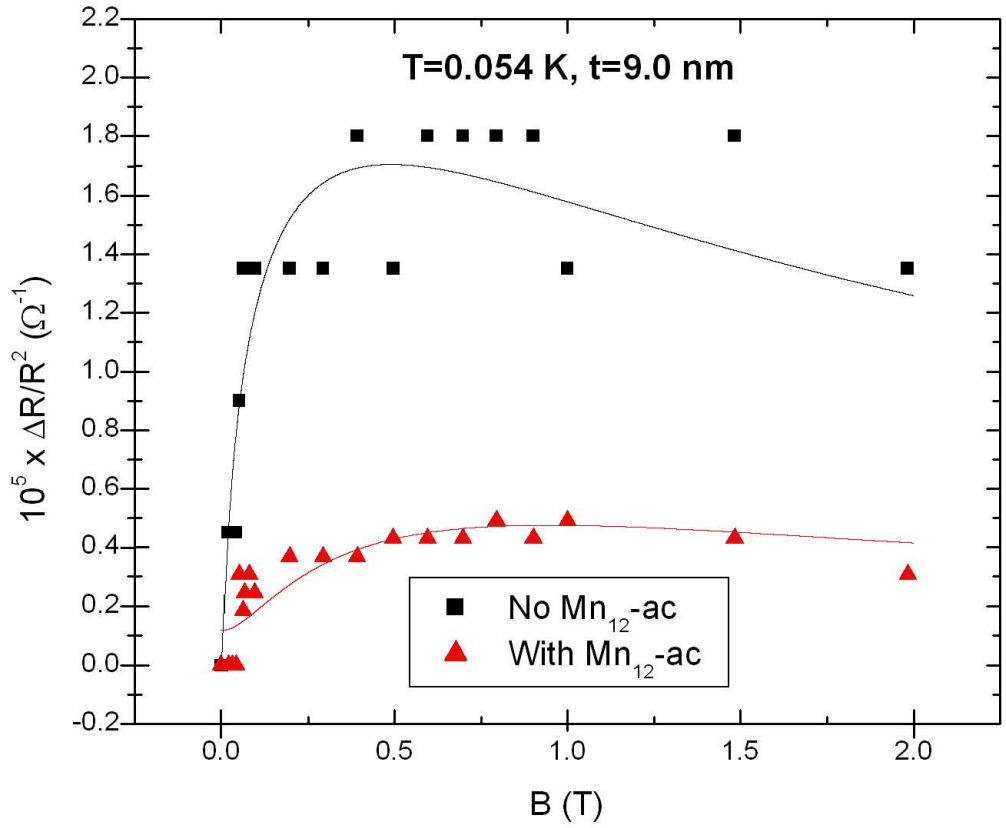

Figure 18: Magnetoresistance of 9.0 nm Au film at 54 mK. Solid curves are fits to theory.

Table 3: Characteristic fields and scattering times for 9.0 nm gold film at 54 mK.

	No Mn_{12}–ac	With Mn_{12}–ac
H_0	1.2±0.2	0.30±0.01
H_i	0.002±0.001	0.021±0.002
H_{so}	0.11±0.01	0.10±0.01
H_s	0.0010±0.0005	0.0025±0.0005
τ_0	$(1.21\pm0.10)\times10^{-15}$	$(2.39\pm0.04)\times10^{-15}$
τ_i	$(9.13\pm3.98)\times10^{-12}$	$(3.43\pm0.27)\times10^{-13}$
τ_{so}	$(1.30\pm0.01)\times10^{-14}$	$(7.21\pm0.60)\times10^{-14}$
τ_s	$(1.82\pm0.79)\times10^{-11}$	$(2.97\pm0.55)\times10^{-12}$

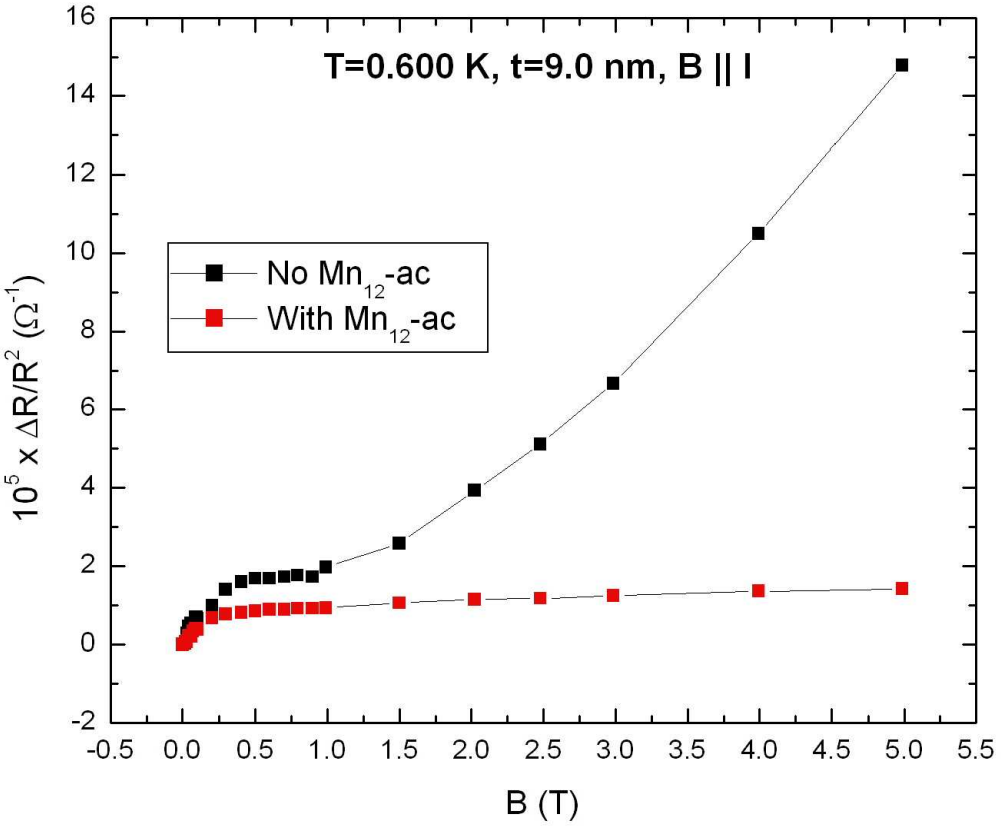

Figure 19: Magnetoresistance of 9.0 nm Au film at 600 mK in a parallel magnetic field. Solid lines are guides to the eye.

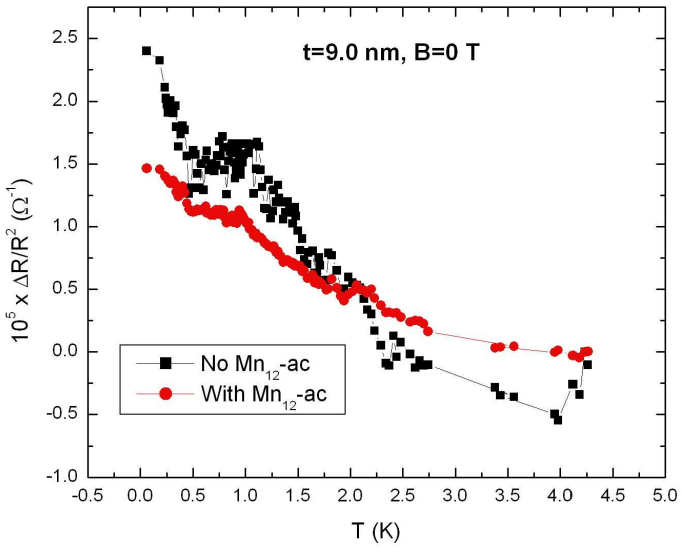

Figure 20: Temperature dependence of resistance of 9.0 nm Au film at 0 T .

of the Mn_{12}–ac. If the effects being seen were due to magnetic field effects, one would expect to see an anomaly at the blocking temperature, where there is a maximum in the magnetization of the Mn_{12}–ac. However, the curve containing the full data (which can be seen in appendix G) shows no anomaly at 3 K which can be discerned within the noise. This lends support to the idea that the changes in the magnetoresistance are due to electronic interactions with the Mn_{12}–ac rather than magnetic field effects.

Figure 21 shows the same curve in a field of 3 T, obtained on cooling back down from 4 K. The curve shows a very similar shape to that taken in zero field.

While data were taken for samples of other thicknesses and at other temperatures, quantitative fits were not always achieved. Figure 22 shows a thinner sample (5.8 nm). While the correlation factors for the fits are reasonable (see table 4), the shape of the curve beyond $\sim$1 T is not captured well by the fit. Qualitatively, however, the behavior is similar to that seen in the other samples presented. In the case of thicker samples (11.0 nm, 13.0 nm), the same can be said. It is possible that the thinner sample was approaching the

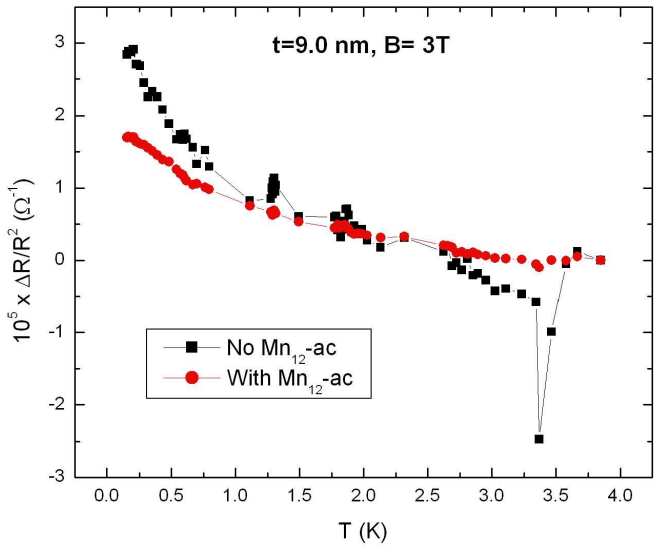

Figure 21: Temperature dependence of resistance of 9.0 nm Au film at 3 T .

percolation regime, where the given theory of weak localization can no longer be applied. For the thicker samples, it is likely that they are moving into the three-dimensional regime. Again, the provided theory of weak localization cannot be applied in this case. In fact, the elastic scattering time noted above for the 9.0 nm film at 600 mK indicates an elastic mean free path of $\sim$10.5 nm. For plots of the acquired data for these and other samples, please see appendix G.

In order to show that the effects being seen are due to Mn_{12}–ac, a control experiment was performed which involved placing only isopropyl alcohol on the surface of the gold film. This was done using the same drop-and-dry method as the Mn_{12}–ac deposition, but without the Mn_{12}–ac added to the isopropyl alcohol. This was done on a 9.0 nm Au film and measured at 600 mK. Figure 23 shows the data obtained for this sample. The fitting parameters for the theoretical curves in the figure are found in table 5. Within experimental error, there is no measurable change in the properties of the Au due to the presence of the

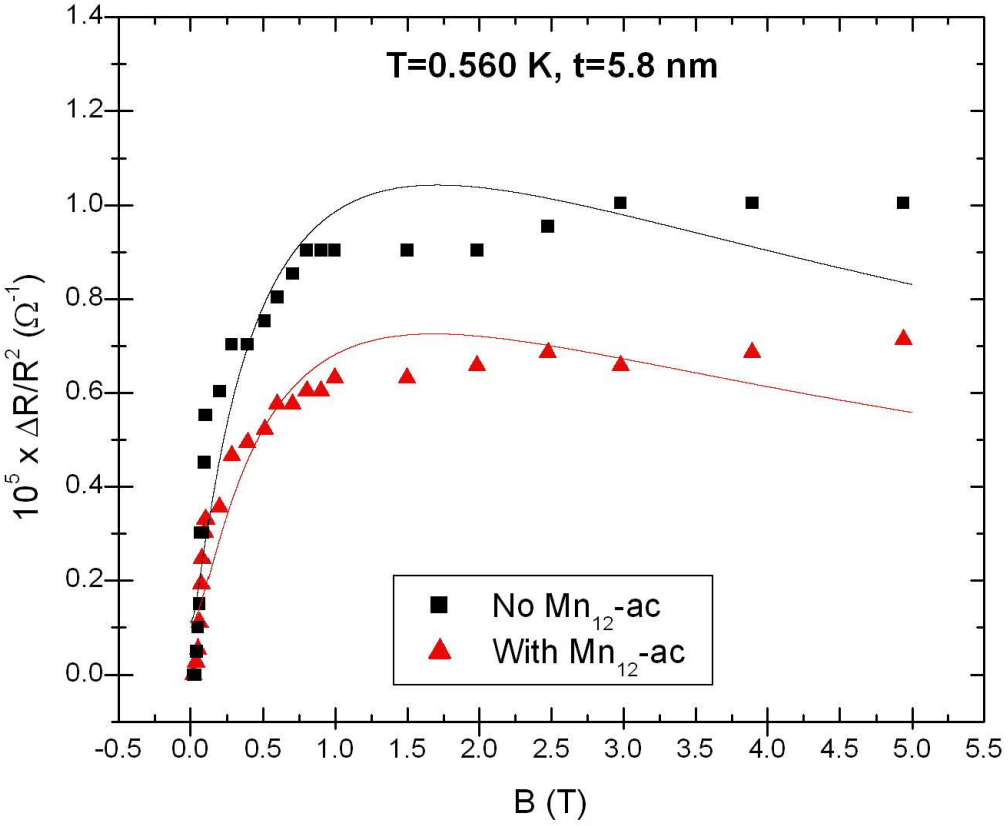

Figure 22: Magnetoresistance of 5.8 nm Au film at 560 mK. Solid curves are fits to theory.

Table 4: Characteristic fields and scattering times for 5.8 nm gold film at 560 mK.

	No Mn_{12}–ac	With Mn_{12}–ac
H_0	1.8±0.1	1.2±0.1
H_i	0.0190±0.0045	0.0180±0.0035
H_{so}	0.33±0.01	0.32±0.03
H_s	0.0015±0.0005	0.0150±0.0040
τ_0	$(9.74\pm0.26)\times10^{-15}$	$(1.20\pm0.05)\times10^{-14}$
τ_i	$(9.68\pm2.02)\times10^{-13}$	$(8.19\pm1.26)\times10^{-13}$
τ_{so}	$(5.31\pm0.02)\times10^{-14}$	$(4.48\pm0.24)\times10^{-14}$
τ_s	$(1.30\pm0.40)\times10^{-11}$	$(1.02\pm2.33)\times10^{-12}$

isopropyl alcohol. From this, it can be concluded that the effects seen are due to the Mn_{12}–ac or some other product within the Mn_{12}–ac / isopropyl alcohol solution.

While the producer of the Mn_{12}–ac used in these experiments claims 100% purity for the powder [75], it is possible that there could be some unreacted manganese acetate clusters remaining in the solution. In order to explore the possibility that the effects seen in the given data are due to some impurity, rather than the Mn_{12}–ac, a sample was prepared using a solution of Mn(II)–ac in isopropanol and deionized water. The Mn(II)-ac molecule was chosen because it is one of the reagents used in the production on Mn_{12}–ac. 11.4 mg of Mn(II)–ac was dissolved in 5 ml of isopropyl alcohol and 5 ml of deionized H_2O. This solution was deposited in the same manner as the Mn_{12}–ac solution onto a 9.0 nm Au film. The magnetoresistance of this sample was measured at 600 mK. Figure 24 shows the data obtained as well as two different theoretical fits. The solid curves are the best fits to the data in a least-squares sense. Fitting parameters for these curves are found in table 6. However, these curves fail to capture the shape of the data at high field. The theoretical fits can be constrained such that the shape is captured, but the fits still deviate significantly at high field. These fits are represented by the dashed curves and the fitting parameters for these curves are found in table 7. Within experimental error, the least-squares fitting parameters show no measurable difference with and without Mn(II)-ac on the surface of the Au film. The constrained fits show some changes due to the presence of the Mn(II)-ac. The elastic scattering time is slightly increased, while the inelastic and spin scattering times are decreased. The amount of change is considerably less than what is seen for the samples with Mn_{12}–ac. Due to the poor nature of the theoretical fits, these scattering times should not be given too much weight. This is, however, strong evidence in support of the fact that Mn_{12}–ac is the main contributor to the changes seen in the magnetoresistance of the Au films presented. Several attempts were made to repeat this measurement with other

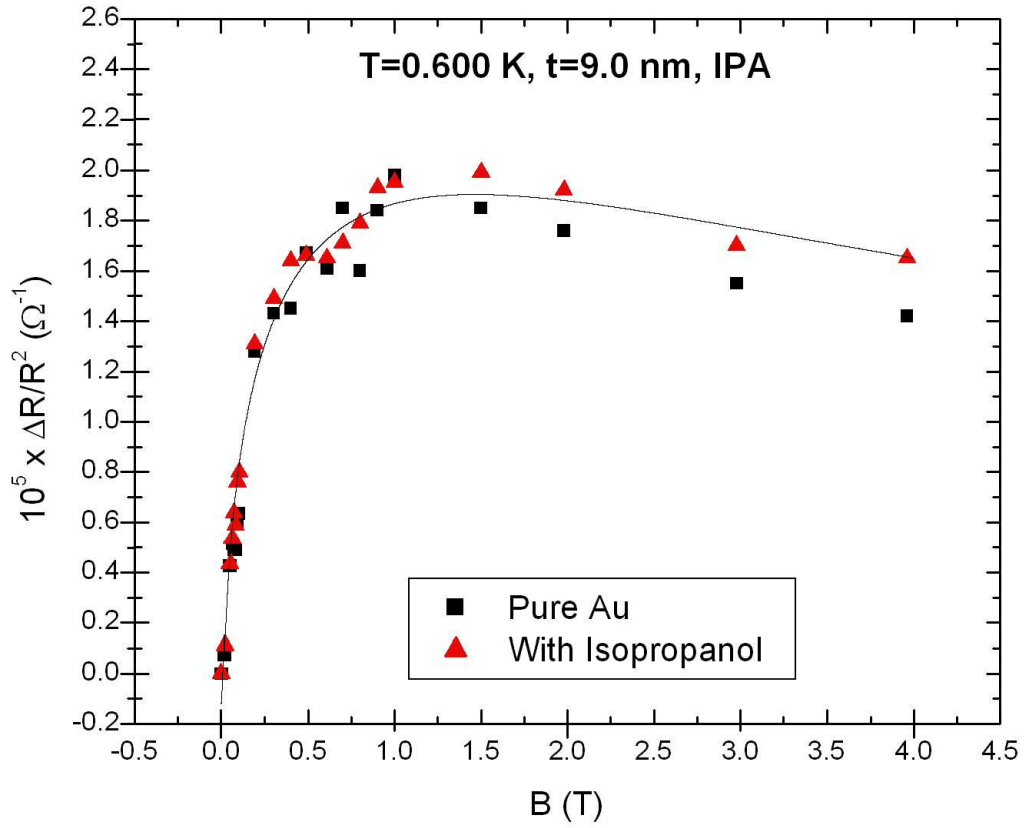

Figure 23: Magnetoresistance of 9.0 nm Au film at 600 mK with isopropyl alcohol. Solid curves are fits to theory. Note that the theoretical curves overlap.

Table 5: Characteristic fields and scattering times for 9.0 nm gold film at 600 mK with isopropyl alcohol.

	No Mn_{12}–ac	With Mn_{12}–ac
H_0	3.0±0.2	3.6±0.4
H_i	0.002±0.0015	0.0015±0.0010
H_{so}	0.27±0.02	0.30±0.02
H_s	0.0010±0.0005	0.0010±0.0005
τ_0	$(7.55\pm0.25)\times10^{-15}$	$(6.92\pm0.38)\times10^{-15}$
τ_i	$(2.52\pm1.85)\times10^{-11}$	$(2.86\pm1.81)\times10^{-11}$
τ_{so}	$(8.40\pm0.34)\times10^{-14}$	$(8.25\pm0.09)\times10^{-14}$
τ_s	$(2.97\pm1.40)\times10^{-11}$	$(3.21\pm1.46)\times10^{-11}$

samples, but problems with the experimental setup, combined with time constraints, did not allow that to be done.

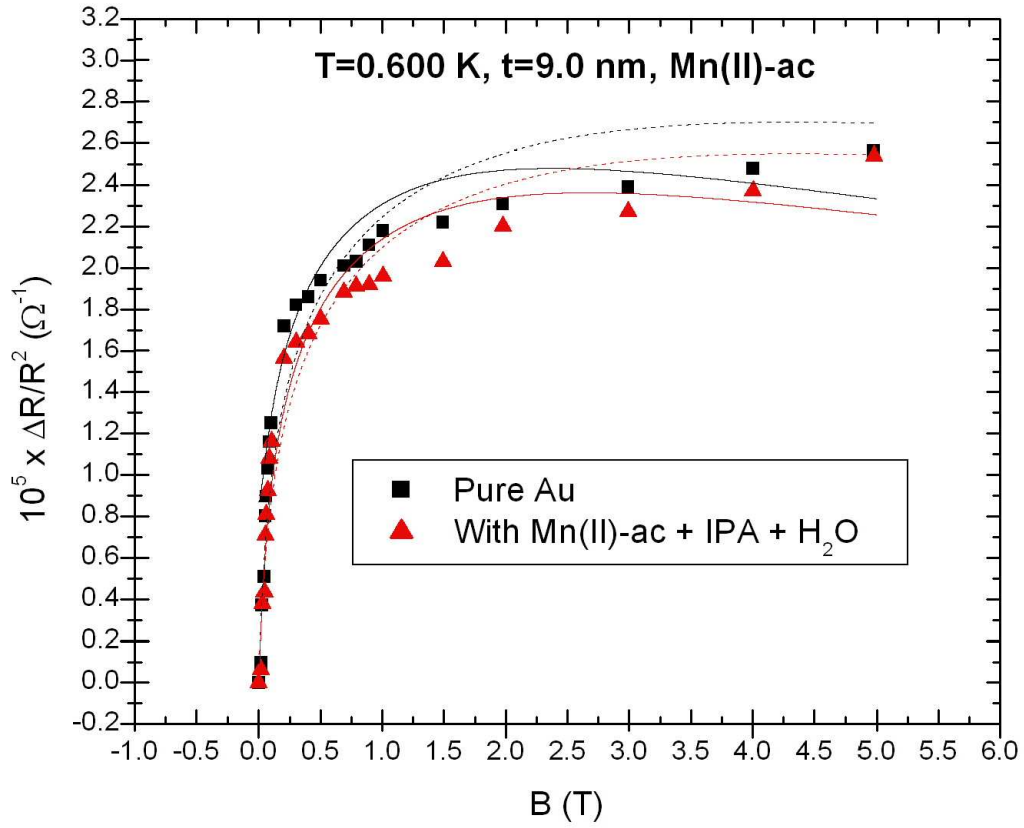

Figure 24: Magnetoresistance of 9.0 nm Au film at 600 mK with Mn(II)-ac. Solid curves are least-squares fits to theory. Dashed curves are fits constrained to match shape of data at high field.

Table 6: Characteristic fields and scattering times for 9.0 nm gold film at 600 mK with Mn(II)–ac (least-squares fit).

	No Mn_{12}–ac	With Mn_{12}–ac
H_0	9.9±0.5	9.9±0.6
H_i	0.0010±0.0005	0.0020±0.0010
H_{so}	0.50±0.02	0.55±0.03
H_s	0.0010±0.0005	0.0010±0.0005
τ_0	$(4.15\pm0.10)\times10^{-15}$	$(4.15\pm0.12)\times10^{-15}$
τ_i	$(5.38\pm2.63)\times10^{-11}$	$(2.68\pm1.27)\times10^{-11}$
τ_{so}	$(8.22\pm0.12)\times10^{-14}$	$(7.48\pm0.18)\times10^{-14}$
τ_s	$(5.52\pm2.70)\times10^{-11}$	$(5.52\pm2.70)\times10^{-11}$

Table 7: Characteristic fields and scattering times for 9.0 nm gold film at 600 mK with Mn(II)–ac (constrained fit).

	No Mn_{12}–ac	With Mn_{12}–ac
H_0	21.6±0.5	19.0±0.1
H_i	0.0015±0.0005	0.0025±0.0020
H_{so}	0.90±0.01	0.90±0.01
H_s	0.0015±0.0005	0.0015±0.0010
τ_0	$(2.81\pm0.03)\times10^{-15}$	$(3.00\pm0.01)\times10^{-15}$
τ_i	$(4.03\pm2.03)\times10^{-11}$	$(1.20\pm0.06)\times10^{-11}$
τ_{so}	$(6.74\pm0.01)\times10^{-14}$	$(6.33\pm0.05)\times10^{-14}$
τ_s	$(4.03\pm2.03)\times10^{-11}$	$(1.71\pm0.57)\times10^{-11}$

CHAPTER VII

CONCLUSION

The purpose of this dissertation is to provide insight into the effect that Mn_{12}–ac has on the electronic transport properties of thin gold films. It has been shown that the presence of the Mn_{12}–ac on the surface of the gold affects significant changes in the magnetoresistance of the gold. Due to the significant amount of noise in the data, as well as problems with reproducibility, the quantitative results presented should not be given too much weight. However, the qualitative changes seen in all samples due to the presence on Mn_{12}–ac were fully reproducible. The quantitative fits to the data from the theory of weak localization indicate that the Mn_{12}–ac reduces the amount of elastic scattering events taking place while adding a significant amount of spin scattering events. This is consistent with a physical picture in which electrons which would normally scatter from the surface of the gold (an elastic scattering event) instead enter the Mn_{12}–ac on the surface and undergo spin scattering from the Mn atoms within the molecular magnets. This result is quite interesting, as it indicates penetration of the electrons from the gold all the way through the acetate ligands to the Mn core of the Mn_{12}–ac molecules. The effect seems to be more prevalent at lower temperatures, but there does not seem to be any indication of a significant change at the blocking temperature of the Mn_{12}–ac.

In the future, further study of these phenomena would be interesting. A more detailed look at the dependence of the various scattering times on the thickness of the gold film is in order. More work to reduce noise in the system would allow a better quantitative picture of the influence of the Mn_{12}-ac molecules on the transport properties of the conduction electrons within the Au films. Also, a look at how the film reacts in a parallel magnetic field could yield further understanding of the interaction mechanisms at work. The use

of a second magnet, with an orientation perpendicular to that currently used, would allow studies of the parallel magnetoresistance like those outlined in ref. [56].

REFERENCES

[1] T. Lis, Acta Cryst. **B 36**, 2042 (1980).

[2] J. Villain, F. Hartman-Boutron, R. Sessoli, and A. Rettori, Europhys. Lett. **27**, 159 (1994).

[3] P. Politi, A. Rettori, F. Hartmann-Boutron, and J. Villain, Phys. Rev. Lett. **75**, 537 (1995).

[4] D. A. Garanin and E. M. Chudnovsky, Phys. Rev. B **56**, 11102 (1997).

[5] Z. Zeng, D. Guenzburger, and D. E. Ellis, Phys. Rev. B **59**, 6927 (1999).

[6] T. Goto, T. Kubo, T. Koshiba, Y. Fujii, A. Oyamada, *et al.*, Physica B: Cond. Mat. **284-288, Part 2**, 1227 (2000).

[7] T. Pohjola and H. Schoeller, Physica B: Cond. Mat. **284-288, Part 2**, 1223 (2000).

[8] J. Tejada, Polyhedron **20**, 1751 (2001).

[9] J. Liu, B. Wu, L. Fu, R. B. Diener, and Q. Niu, Phys. Rev. B **65**, 224401 (2002).

[10] M. R. Pederson, N. Bernstein, and J. Kortus, Phys. Rev. Lett. **89**, 097202 (2002).

[11] A. V. Postnikov, J. Kortus, and M. R. Pederson, Phys. Status Solidi B **243**, 2533 (2006).

[12] J. Kortus, C. R. Chim. **10**, 65 (2007).

[13] A. Caneschi, D. Gatteschi, R. Sessoli, A. L. Barra, L. C. Brunel, *et al.*, J. Am. Chem. Soc. **113**, 5873 (1991).

[14] R. Sessoli, D. Gatteschi, A. Caneschi, and M. A. Novak, Nature **365**, 141 (1993).

[15] B. Barbara, W. Wernsdorfer, L. Sampaio, J.-G. Park, C. Paulsen, *et al.*, J. Magn. Magn. Mater. **140-144**, 1825 (1995).

[16] C. Paulsen and J.-G. Park, in *Quantum Tunneling of Magnetization - QTM '94*, edited by L. Gunther and B. Barbara (Kluwer Academic Publishers, Dordrecht, the Netherlands, 1995), pp. 189–207.

[17] C. Paulsen, J.-G. Park, B. Barbara, R. Sessoli, and A. Caneschi, J. Magn. Magn. Mater. **140-144**, 379 (1995).

[18] M. A. Novak and R. Sessoli, in *Quantum Tunneling of Magnetization - QTM '94*, edited by L. Gunther and B. Barbara (Kluwer Academic Publishers, Dordrecht, the Netherlands, 1995), pp. 171–188.

[19] M. A. Novak, R. Sessoli, A. Caneschi, and D. Gatteschi, J. Magn. Magn. Mater. **146**, 211 (1995).

[20] B. Barbara, L. Thomas, F. Lionti, I. Chiorescu, and A. Sulpice, J. Magn. Magn. Mater. **200**, 167 (1999).

[21] J. R. Friedman, M. P. Sarachik, J. Tejada, and R. Ziolo, Phys. Rev. Lett. **76**, 3830 (1996).

[22] M.-H. Jo, J. Grose, K. Baheti, M. Deshmukh, J. Sokol, *et al.*, Nano Lett. **6**, 2014 (2006).

[23] M. N. Leuenberger and E. R. Mucciolo, Phys. Rev. Lett. **97**, 126601 (2006).

[24] H. B. Heersche, Z. de Groot, J. A. Folk, H. S. J. van der Zant, C. Romeike, *et al.*, Phys. Rev. Lett. **96**, 206801 (2006).

[25] C. Ni, S. Shah, D. Hendrickson, and P. R. Bandaru, Appl. Phys. Lett. **89**, 212104 (2006).

[26] C. Romeike, M. R. Wegewijs, W. Hofstetter, and H. Schoeller, Phys. Rev. Lett. **97**, 206601 (2006).

[27] S. Voss, M. Fonin, U. Rudiger, M. Burgert, and U. Groth, Appl. Phys. Lett. **90**, 133104 (2007).

[28] M. Cavallini, F. Biscarini, J. Gómez-Segura, D. Ruiz, and J. Veciana, Nano Lett. **3**, 1527 (2003).

[29] A. Cornia, A. C. Fabretti, M. Pacchioni, L. Zobbi, D. Bonacchi, *et al.*, Angew. Chem. Int. Ed. **42**, 1645 (2003).

[30] D. Ruiz-Molina, M. Mas-Torrent, J. Gómez, A. I. Balana, N. Domingo, *et al.*, Adv. Mater. **15**, 42 (2003).

[31] M. Clemente-León, H. Soyer, E. Coronado, C. Mingotaud, C. J. Gómez-García, *et al.*, Angew. Chem. Int. Ed. **37**, 2842 (1998).

[32] M. Autric, T. Itina, W. Marine, and F. Grangeon, in *Proceedings of SPIE-The International Society for Optical Engineering, v. 3574 (XII International Symposium on Gas Flow and Chemical Lasers and High-Power Laser Conference, 1998)*, edited by A. S. Boreisho and G. A. Baranov, European Optical Society (SPIE–the International Society for Optical Engineering, Bellingham, Washington, 1998), pp. 415–425.

[33] J. Means, V. Meenakshi, R. Srivastava, W. Teizer, A. Kolomenskii, *et al.*, J. Magn. Magn. Mater. **284**, 215 (2004).

[34] V. Meenakshi, W. Teizer, K. D. D. Rathnayaka, D. Naugle, H. Zhao, *et al.*, APS Bull. **48**, 1019 (2003).

[35] V. Meenakshi, W. Teizer, D. Naugle, H. Zhao, and K. Dunbar, Solid State Comm. **132**, 471 (2004).

[36] D. Seo, V. Meenakshi, W. Teizer, H. Zhao, and K. Dunbar, J. Magn. Magn. Mater. **301**, 31 (2006).

[37] K. Kim, D. M. Seo, J. Means, V. Meenakshi, W. Teizer, *et al.*, Appl. Phys. Lett. **85**, 3872 (2004).

[38] I. Tupitsyn and B. Barbara, in *Magnetism: Molecules to Materials III*, edited by J. S. Miller and M. Drillon (Wiley-VCH Verlag GmbH, Weinheim, 2002), p. 109.

[39] J. A. A. J. Perenboom, J. S. Brooks, S. Hill, T. Hathaway, and N. S. Dalal, Phys. Rev. B **58**, 330 (1998).

[40] E. M. Chudnovsky and L. Gunther, Phys. Rev. Lett. **60**, 661 (1988).

[41] M. Enz and R. Schilling, J. Phys. C **19**, 1765 (1986).

[42] J. L. van Hemmen and A. Suto, Europhys. Lett. **1**, 481 (1986).

[43] P. C. E. Stamp, Phys. Rev. Lett. **66**, 2802 (1991).

[44] E. M. Chudnovsky, J. Magn. Magn. Mater. **140-144**, 1821 (1995).

[45] A. Caneschi, T. Ohm, C. Paulsen, D. Royal, C. Sangregorio, *et al.*, J. Magn. Magn. Mater. **177-181**, 1330 (1998).

[46] L. Thomas, F. Lionti, R. Ballou, D. Gatteschi, R. Sessoli, *et al.*, Nature **383**, 145 (1996).

[47] J. M. Hernandez, X. X. Zhang, F. Luis, J. Tejada, J. R. Friedman, *et al.*, Phys. Rev. B **55**, 5858 (1997).

[48] V. L. Pokrovsky, private communications.

[49] P. Kapitza, Proc. Roy. Soc. (London) **123**, 292 (1929).

[50] C. Kittel, *Quantum Theory of Solids* (John Wiley & Sons, New York, 1987), 2nd ed.

[51] E. Abrahams, P. W. Anderson, D. C. Licciardello, and T. V. Ramakrishnan, Phys. Rev. Lett. **42**, 673 (1979).

[52] P. A. Lee and T. V. Ramakrishnan, Phys. Rev. B **26**, 4009 (1982).

[53] S. Hikami, A. I. Larkin, and Y. Nagaoka, Prog. Theor. Phys. **63**, 707 (1980).

[54] G. Bergmann, Phys. Rev. B **28**, 2914 (1983).

[55] G. Bergman, Phys. Rev. Lett. **48**, 1046 (1982).

[56] N. Giordano and M. A. Pennington, Phys. Rev. B **47**, 9693 (1993).

[57] V. Bayot, L. Piraux, J.-P. Michenaud, J.-P. Issi, M. Lelaurain, *et al.*, Phys. Rev. B **41**, 11770 (1990).

[58] H. Beckmann, R. Schäfer, W. Li, and G. Bergmann, Europhys. Lett. **33**, 563 (1996).

[59] H. Beckmann and G. Bergmann, Phys. Rev. B **55**, 14350 (1997).

[60] A. M. Kreshchuk, S. V. Novikov, T. A. Polyanskaya, and I. G. Savel'ev, Semicond. Sci. Technol. **13**, 384 (1998).

[61] J. Dai and J. Tang, J. Appl. Phys. **92**, 6047 (2002).

[62] Y. Wang and J. J. Santiago-Aviles, J. Appl. Phys. **94**, 1721 (2003).

[63] G. M. Minkov, A. V. Germanenko, and I. V. Gornyi, Phys. Rev. B **70**, 245423 (2004).

[64] S. McPhail, C. E. Yasin, A. R. Hamilton, M. Y. Simmons, E. H. Linfield, *et al.*, Phys. Rev. B **70**, 245311 (2004).

[65] P. Lang, V. S. Stepanyuk, K. Wildberger, R. Zeller, and P. H. Dederichs, Solid State Comm. **92**, 755 (1994).

[66] H. Beckmann, F. Ye, and G. Bergmann, Phys. Rev. Lett. **73**, 1715 (1994).

[67] C. D. Wagner, A. V. Naumkin, A. Kraut-Vass, J. W. Allison, C. J. Powell, *et al.*, NIST X-ray Photoelectron Spectroscopy Database, http://srdata.nist.gov/xps/ (2006).

[68] J.-S. Kang, J. H. Kim, Y. J. Kim, W. S. Jeon, D.-Y. Jung, *et al.*, J. Korean Phys. Soc. **40**, L402 (2002).

[69] V. Di Castro and G. Polzonetti, J. Electron Spectrosc. Relat. Phenom. **48**, 117 (1989).

[70] W. S. Seo, H. H. Jo, K. Lee, B. Kim, S. J. Oh, *et al.*, Angew. Chem. Int. Ed. **43**, 1115 (2004).

[71] G. Lee, S. Huh, J. Jeong, B. Choi, S. Kim, *et al.*, J. Am. Chem. Soc. **124**, 12094 (2002), ISSN 0002-7863.

[72] O. V. Lounasmaa, *Experimental Principles and Methods Below 1 K* (Academic Press, New York, 1974).

[73] F. Pobell, *Matter and Methods at Low Temperatures* (Springer, Berlin, 2007), 3rd ed.

[74] E. L. Ziercher, K. I. Blum, and Y. Hu, in *Experimental Techniques in Condensed Matter Physics at Low Temperatures*, edited by R. C. Richardson and E. N. Smith (Addison-Wesley, Reading, Massachusetts, 1988), chap. 5, pp. 287–320.

[75] H. Zhao, private communications.

APPENDIX A

WIRING DIAGRAMS FOR DILUTION REFRIGERATOR

Keithley 2700/7700 Multimeter/Scanner

One item purchased for use with the dilution refrigerator was a Keithley model 2700 Multimeter/Switch System with a model 7700 20-channel Multiplexer Module. Part of the initial intent was to use seven of the channels to read 2-wire resistances of the diagnostic thermometers within the dilution refrigerator (see section on Thermometry in chapter V). As it turned out, the power input from the 2700 was high enough to cause significant heating of the thermometers, rendering an incorrect reading. This explains the design of the interface box which I designed to be used with this multimeter, but not it's use. Another design choice that didn't work out has to do with the "Lock-in" inputs. For each of three "Lock-in" inputs, there are three terminals, marked "V+", "V-", and "Out". The original intent was for "V+" and "V-" to be connected across the current-limiting resistor used between the oscillator output of the lock-in and the current leads on a sample. The "Out" terminal is for the DC monitor output of the lock-in. By measuring the actual voltage drop across the current-limiting resistor, one can calculate the input current to the sample, allowing precise determination of the resistance. In practice, however, the AC voltage measurement (between "V+" and "V-") causes a sharp drop in the actual current being sent to the sample. This is due to the fact that the input resistance of the 2700 for AC voltage measurements is 1 MΩ. When using a 100 kΩ or 1 MΩ current-limiting resistor, a significant portion of the current will be going to the Keithley 2700 rather than the sample.

In addition to the three sets of "Lock-in" terminals, the front panel of the interface box has one 50-pin centronics socket (labeled "CEN 1") and seven pairs of binding posts (labeled "Ch 1" – "Ch 7"). The rear panel has two 50-pin centronics sockets ("CEN 2" and

"CEN 3"), one 5-pin connector ("C/G Res."), one pair of banana terminals ("Heater") and five pair of binding posts ("Input", "Sense", "Amps Com", "Amps21", and "Amps22"). The purpose of "CEN 1" is to accept a wiring harness coming from the dilution refrigerator with the mating centronics plug. This contains the wires for the seven diagnostic thermometers, the wires for a heater in the mixing chamber and the wires for a carbon glass thermometer mounted on the mixing chamber stage. "CEN 2" accepts a wiring harness which is terminated on the Keithley 7700 module. The "C/G Res." and "Heater" terminals accept plugs which go to the aforementioned mixing chamber heater and carbon glass thermometer. These plugs originally plugged into the back of a home-built resistance bridge which accepted the centronics plug on the harness coming from the dilution refrigerator. Table 8 lists the connections to connector "CEN 2" from other terminals on the interface box as well as the corresponding channel number on the Keithley 7700 module. For information on what the unnumbered channels are for, one can consult the Operator's Manual for the Keithley 2700.

Diagnostic Thermometer Breakout Panel

Since the measurement of the diagnostic thermometers with the Keithley 2700/7700 setup did not work effectively, I also built a breakout panel to allow easy access to the wires for the diagnostic thermometers from the wiring bundle with the 50-pin centronics plug mentioned above. This panel consists of 25 pairs of binding posts and one 50-pin centronics socket. While I did not connect all of the wires from the centronics socket to the binding posts, I did break out all of the wires needed to measure the seven diagnostic thermometers as well as the two wires which go to the mixing chamber heater. Assuming the bottom row of binding post pairs is numbered from one to eleven, left to right, table 9 lists the connections made on this panel (the top row is not wired at all).

Table 8: Wiring for Keithley 2700/7700 DMM/Scanner.

CEN 2	Interface Box	7700 Channel
1	Ch 1+	1+
2	Ch 1-	1-
3	Ch 2+	2+
4	Ch 2-	2-
5	Ch 3+	3+
6	Ch 3-	3-
7	Ch 4+	4+
8	Ch 4-	4-
9	Ch 5+	5+
10	Ch 5-	5-
11	Ch 6+	6+
12	Ch 6-	6-
13	Ch 7+	7+
14	Ch 7-	7-
15	Lock-in 1: V+ inner	8+
16	Lock-in 1: V– inner	8-
17	Lock-in 1: Out inner	9+
18	Lock-in 1: Out outer	9-
19	Lock-in 2: V+ inner	10+
20	Lock-in 2: V– inner	10-
21	Lock-in 2: Out inner	11+
22	Lock-in 2: Out outer	11-
23	Lock-in 3: V+ inner	12+
24	Lock-in 3: V– inner	12-
25	Lock-in 3:Out inner	13+

CEN 2	Interface Box	7700 Channel
26	Lock-in 3: Out outer	13-
27	CEN1: 1	14+
28	CEN1: 4	14-
29	CEN1: 5	15+
30	CEN1: 8	15-
31	CEN1: 9	16+
32	CEN1: 12	16-
33	CEN1: 13	17+
34	CEN1: 16	17-
35	CEN1: 17	18+
36	CEN1: 20	18-
37	CEN1: 21	19+
38	CEN1: 24	19-
39	CEN1: 26	20+
40	CEN1: 29	20-
41	Input +	Input +
42	Input -	Input -
43	Sense +	Sense +
44	Sense -	Sense -
45	Amps Com +	Amps Com +
46	Amps Com -	Amps Com -
47	Amps21 +	Amps21 +
48	Amps21-	Amps21-
49	Amps22+	Amps22+
50	Amps22-	Amps22-

Table 9: Wiring for diagnostic thermometer breakout panel.

Binding Posts	Centronics Pin #'s	Purpose
1	1, 4	R1: 1K Pot
2	2, 3	
3	5, 8	R2: Still
4	6, 7	
5	9, 12	R3: Heat Exch. 1
6	10, 11	
7	13, 16	R4: Heat Exch. 3
8	14, 15	
9	17, 20	R5: Heat Exch. 5
10	18, 19	Mixing Chamber Heater
11	21, 24	R6: Heat Exch. 6
12	22, 23	
13	25, 28	R7: Mixing Chamber
14	none (would be 26, 27)	

Sample Wiring

A major part of starting the operation of the dilution refrigerator was tracing the sample wiring from the cold finger to a board on the equipment rack with 40 BNC connectors. After the connections were established, over time, some of the wires broke at the sample mounts. Eventually, the wiring from the mixing chamber stage to the sample mounts on the end of the cold finger were re-worked (not completely replaced, but the broken wires were fixed). Table 10 tabulates the connections from the board on the equipment rack (rows A, B, C, and D, each with ten connectors) and the corresponding label number on the wire at the sample stage. The two connections labeled "C_{in}" are for the carbon resistor mounted inside the vacuum can for diagnostic purposes during cool down.

Table 10: Dilution refrigerator sample wiring.

	1	2	3	4	5	6	7	8	9	10
A	1-5	1-6	3-1	3-2	4-3	4-4	1-1	1-2	1-3	1-4
B	C_{in}	1-8	1-9	1-10	2-1	2-2	2-4	2-3	2-5	2-6
C	2-7	2-8	2-9	2-10	C_{in}	3-4	3-5	3-6	3-7	3-8
D	3-9	3-10	4-1	4-2	4-5	4-6	4-7	4-8	4-9	4-10

APPENDIX B

COOLDOWN PROCEDURE

1. Initial:

    - Check all electrical leads.
    - Put up radiation shield.
    - Recheck all electrical leads.
    - Put up vacuum can.
    - Recheck all electrical leads.
    - Leak check vacuum can.
    - Pump on vacuum can for ~1hr. with small diffusion pump.
    - Pump with small diffusion pump on both sides of circulation system for ~1hr.
    - Hang superconducting magnet.
    - Attach V-sense and heater leads to magnet.
    - Attach superconducting level meters (top and bottom).
    - Attach heater to bottom of vacuum can.
    - Attach extension to LHe fill line.
    - Tape leads out of the way.
    - Put up dewar and tighten bolts.
    - Open 1K fill valve.
    - Pump out dewar for at least 1/2 hour.
    - When pressure is low in dewar, open 1K pumping line.

2. Precool:

   - Stop pumping on circulation system and vacuum can.
   - Add ^{3}He exchange gas to vacuum can.
   - Fill circulation system LN_2 cold trap.
   - Circulation check:
     - Make sure pumping side of circulation system is < 1mT.
     - Put mixture on return side of circulation system (circulate through cold trap before opening last valve to circulation system).
     - Measure rise time for pressure on pumping side of circulation system.
   - Close valve to 1K pump.
   - Close 1K fill valve.
   - Fill dewar with N_2 gas.
   - Pressurize 1K pot with ~16 psi He gas.
   - Transfer LN_2.
   - Wait until inside and outside C thermometers show appropriate LN_2 values.
   - Circulation check (same as previous).

3. Cool Down:

   - Back transfer LN_2:
     - Make sure transfer tube is fully seated in extension.
     - Pressurize dewar with N_2 gas to push out liquid from bottom of dewar.
   - Pump out dewar until pressure reaches $\sim$-30.

- Back fill dewar with He gas.
- Transfer LHe until upper level meter reads $\sim$70%.
- Pump out vacuum can.
- Open 1K pumping line and pump out 1K pot.
- Open 1K fill valve. Pressure should rise then stop.
- Close 1K fill valve when pressure rises again.
- Add mixture to pumping side of circulation system and allow it to condense into the system.
- Once pressure on pumping side has stabilized, open return side valve and begin pumping to start circulation.
- Once the temperature is < 600 mK, turn on still heater to improve cooling speed.

APPENDIX C

DATA FITTING

Fitting of experimental data with the theoretical equations given in chapter III was done using a least-squares fitting method. This method determines the best fit by calculating the "sum of squares" error (SSerr) for each possible set of parameters and taking the set with the minimum error. The sum of squares error is found by taking the difference between the calculated value of the function at a given point and the measured value at that point, and squaring that difference. This square of the difference is then summed up for all of the given data points. The least-squares solution is the set of parameters which give the lowest sum of squares error. Another measure of the quality of the fit, besides SSerr, is the correlation factor, R^2, which is given as

$$R^2 = 1 - \frac{SSerr}{SStot}$$

where SStot is the sum of the squares of the differences between the data points and the mean of all of the data points. This correlation factor, then, gives extra weight to the ability of the proposed fit to match data which vary greatly from the mean value. A correlation factor of unity is a perfect fit. The closer R^2 is to unity, the better the fit.

I wrote a C++ program, deltaRfits.cpp, which steps through various values of H_0, H_i, H_{so}, and H_s and calculates the sum of squares error and the correlation factor for the function for $\frac{\Delta R}{R^2}$. Data for the fitting are read in from a tab-separated file with two columns, the first for the magnetic field and the second for $\frac{\Delta R}{R^2}$. This file is named "datafile.txt". Another file, named "limits.txt", contains limits on the values for the characteristic fields and the allowable error. Setting these limits appropriately limits the number of iterations carried out as well as the amount of output given. Possible fits, with a sum of squares

error smaller than the given limit, are output to the file "fit_parameters.txt". This file has six columns containing the four fitting parameters, the sum of squares error and the correlation factor for the fit. The program outputs any new fit which has a smaller error than the previous best fit, thereby converging on the least-squares fit. The code listing is given in appendix D. A variation on this program, deltaRfits_range.cpp (appendix E), outputs all sets of fitting parameters which have an error below the maximum error set in the "limits.txt" file. This allows the user to find a range of possible fitting parameters which will give similar errors. This is how the errors given in the experimental chapter were determined.

Initially, a given set of data were imported into Mathematica (an example notebook is given in appendix F), where an initial curve fitting was done manually. This initial fitting provided a basis for setting the limits for the automated curve fitting. After an initial run of the curve fitting program, if it appeared that the program was still improving its fit when it reached an upper limit on a given parameter, that limit was adjusted and the program allowed to run again. Iterative adjustment of the limit on the error allowed for a limit on the number of possible fits given in the output file. By placing several fits in the output file, instead of simply outputting the least-squares fit, it was possible to get an idea of a range of possible values for the fitting parameters which give similar accuracy, thereby enabling an estimation of the error involved in the fitting parameters. The best-fit parameters were then used in the Mathematica notebook to produce a data file containing the fit (using 10000 points per tesla). These data, along with the original data, were imported into Origin to make the plots given in the text. The Mathematica notebook was also used to calculate the scattering times from the characteristic fields.

APPENDIX D

CODE LISTING

```
/*********************************************************************
Program: deltaRfit_least.cpp
Author:    Joel Means
Date:       27 May, 2007

This program is designed to do a fit to a data set using the equation
for deltaR found in:
N. Giordano and M.A. Pennington, Phys. Rev. B, 47, 9693 (1993).
It will calculate the best fit to the data using the four parameters
H0, Hso, Hi and Hs, based on a least-squares fit.
*********************************************************************/

#include <math.h>
#include <iostream>
#include <fstream>

// digamma(x) calculates the digamma function of x
double digamma(double x){
   double psi;
   if ( x >= 0.5 && x <= 3.0 )
      psi = ( log(x + 1.0)
            - 1.0 / (2.0 * (x + 1.0))
            - 1.0 / (12.0 * pow((x + 1.0), 2))
```

```
            + 1.0 / (120.0 * pow((x + 1.0), 4))
            - 1.0 / (252.0 * pow((x + 1.0), 6))
            - 1.0 / x );
    else if ( x > 3.0 )
        psi = ( log(x)
            - 1.0 / (2.0 * x)
            - 1.0 / (12.0 * pow(x , 2))
            + 1.0 / (120.0 * pow(x , 4))
            - 1.0 / (252.0 * pow(x , 6))
            );
    else
        psi = 0.0;
    return psi;
}

// deltaR(H, Hn[]) calculates deltaR(H) with paramters Hn[] as
// noted in main()
double deltaR(double H, double Hn[]){
    double e = 1.60 * pow(10.,-19);
    double hbar = 1.05457 * pow(10.,-34);
    double pi = 3.14159265;
    double delta = 0.;
    double coeff = 1.;
    double psis= 1.;
    coeff = ( (pow(e , 2)) / (2.0 * pow(pi , 2) * hbar) );
    psis = (digamma((0.5 + Hn[0]/H))
```

```
            - 1.5 * digamma((0.5 + Hn[1]/H))
            + 0.5 * digamma((0.5 + Hn[2]/H)));
    delta = coeff * psis;
    return delta;
}


int main(){
    int i, j, k, l, m, n, p, numDataPoints;
    // For the experimental data that will be read in
    float expH[80], expDeltaR[80];
    double total, mean, fit, ssErr, ssTot;
    double rSquared, highRSquared;
    double meanErr, bigErr, pointErr, lowErr;

    // Min, Max and step sizes for adjustable parameters
    float stepH0   = 0.5;
    float stepHso  = 0.01;
    float stepHi   = 0.0005;
    float stepHs   = 0.0005;

    float maxH0;
    float maxHso;
    float maxHi;
    float maxHs;
```

```
float minH0;
float minHso;
float minHi;
float minHs;

float maxErr;

double charFields[4];    // Characteristic Fields
                         // charFields[0] = H0
                         // charFields[1] = Hso
                         // charFields[2] = Hi
                         // charFields[3] = Hs

double Hn[3];            // Hn[0]=H1, Hn[1]=H2 and Hn[2]=H3

// Initialize the output file
std::ofstream outfile;
outfile.open("fit_parameters.txt", std::fstream::out);
outfile << "H0"<< '\t'
      << "Hso"<< '\t'
      << "Hi"<< '\t'
      << "Hs"<< '\t'
      << "error"<< '\t'
      << "Rsquared"<< std::endl;
outfile.close();
```

```
// Initialize the another output file
std::ofstream outfile2;
outfile2.open("fit_parameters_rsquared.txt",
                std::fstream::out);
outfile2 << "H0"<< '\t'
      << "Hso"<< '\t'
      << "Hi"<< '\t'
      << "Hs"<< '\t'
      << "error"<< '\t'
      << "Rsquared"<< std::endl;
outfile2.close();

// Read in the experimental data from file "datafile.txt"
std::ifstream datafile;
datafile.open("datafile.txt", std::fstream::in);
i=0;
while(datafile >> expH[i] >> expDeltaR[i]){
   i++;
}
datafile.close();
if(expH[0] == 0.){
   expH[0] += .00000001;       // Remove singularity at H=0
}
numDataPoints = i;
p=0;
for(total=0, p=0; p<numDataPoints; p++){
```

```
    expDeltaR[p] *= -1.; // My input files have deltaL = -deltaR
    total += expDeltaR[p];
}

mean = total / numDataPoints;

// Read in limits for fit
std::ifstream limits;
limits.open("limits.txt", std::fstream::in);
limits >> minH0 >> maxH0 >> minHso >> maxHso
       >> minHi >> maxHi >> minHs >> maxHs >> maxErr;
limits.close();

lowErr=maxErr;
highRSquared = 0;

// Step through possible values based on Min, Max and Step Sizes
for(j=(minH0/stepH0); j<=(maxH0/stepH0); j++){
    charFields[0] = (j * stepH0);
    for(k=(minHso/stepHso); k<=(maxHso/stepHso); k++){
        charFields[1] = (k * stepHso);
        for(l=(minHi/stepHi); l<=(maxHi/stepHi); l++){
            charFields[2] = (l * stepHi);
            for(m=(minHs/stepHs); m<=(maxHs/stepHs); m++){
                charFields[3] = (m * stepHs);
```

```
// Set the Hn paramters from the charFields at each step
Hn[0] = ( charFields[0] + charFields[1]
      + charFields[3] );
Hn[1] = ( (4./3.)  * charFields[1]
      + (2./3.)  * charFields[3]
      + charFields[2] );
Hn[2] = ( 2.  * charFields[3]
      + charFields[2] );

ssErr = 0;
ssTot = 0;
bigErr = 0;
outfile.open("fit_parameters.txt",
       std::fstream::out |std::fstream::app);
outfile2.open("fit_parameters_rsquared.txt",
       std::fstream::out |std::fstream::app);
for(n=0; n<numDataPoints; n++){
   fit = deltaR (expH[n], Hn);
   pointErr = pow((fit - expDeltaR[n]),2);
   meanErr = pow((mean - expDeltaR[n]),2);
   ssErr += pointErr;
   ssTot += meanErr;
}
rSquared = 1 - (ssErr / ssTot);
if(ssErr < lowErr){
   outfile << charFields[0] << '\t'
```

```
                        << charFields[1] << '\t'
                        << charFields[2] << '\t'
                        << charFields[3] << '\t'
                        << ssErr << '\t'
                        << rSquared << std::endl;
                    lowErr=ssErr;
                }
                outfile.close();
                if(rSquared > highRSquared){
                    outfile2 << charFields[0] << '\t'
                        << charFields[1] << '\t'
                        << charFields[2] << '\t'
                        << charFields[3] << '\t'
                        << ssErr << '\t'
                        << rSquared << std::endl;
                    highRSquared=rSquared;
                }
                outfile2.close();
            }
        }
    }
}
```

APPENDIX E

CODE LISTING 2

```
/*********************************************************************
Program: deltaRfit_range.cpp
Author:    Joel Means
Date:       27 May, 2007

This program is designed to do a fit to a data set using the equation
for deltaR found in:
N. Giordano and M.A. Pennington, Phys. Rev. B, 47, 9693 (1993).
It will calculate the best fit to the data using the four parameters
H0, Hso, Hi and Hs, based on a least-squares fit.
*********************************************************************/

#include <math.h>
#include <iostream>
#include <fstream>

// digamma(x) calculates the digamma function of x
double digamma(double x){
   double psi;
   if ( x >= 0.5 && x <= 3.0 )
      psi = ( log(x + 1.0)
            - 1.0 / (2.0 * (x + 1.0))
            - 1.0 / (12.0 * pow((x + 1.0), 2))
```

```
            + 1.0 / (120.0 * pow((x + 1.0), 4))
            - 1.0 / (252.0 * pow((x + 1.0), 6))
            - 1.0 / x );
    else if ( x > 3.0 )
        psi = ( log(x)
            - 1.0 / (2.0 * x)
            - 1.0 / (12.0 * pow(x , 2))
            + 1.0 / (120.0 * pow(x , 4))
            - 1.0 / (252.0 * pow(x , 6))
            );
    else
        psi = 0.0;
    return psi;
}

// deltaR(H, Hn[]) calculates deltaR(H) with paramters Hn[] as
// noted in main()
double deltaR(double H, double Hn[]){
    double e = 1.60 * pow(10.,-19);
    double hbar = 1.05457 * pow(10.,-34);
    double pi = 3.14159265;
    double delta = 0.;
    double coeff = 1.;
    double psis= 1.;
    coeff = ( (pow(e , 2)) / (2.0 * pow(pi , 2) * hbar) );
    psis = (digamma((0.5 + Hn[0]/H))
```

```
            - 1.5 * digamma((0.5 + Hn[1]/H))
            + 0.5 * digamma((0.5 + Hn[2]/H)));
    delta = coeff * psis;
    return delta;
}


int main(){
    int i, j, k, l, m, n, p, numDataPoints;
    // For the experimental data that will be read in
    float expH[80], expDeltaR[80];
    double total, mean, fit, ssErr, ssTot;
    double rSquared, highRSquared;
    double meanErr, bigErr, pointErr, lowErr;

    // Min, Max and step sizes for adjustable parameters
    float stepH0   = 0.5;
    float stepHso  = 0.01;
    float stepHi   = 0.0005;
    float stepHs   = 0.0005;

    float maxH0;
    float maxHso;
    float maxHi;
    float maxHs;
```

```
float minH0;
float minHso;
float minHi;
float minHs;

float maxErr;

double charFields[4];    // Characteristic Fields
                         // charFields[0] = H0
                         // charFields[1] = Hso
                         // charFields[2] = Hi
                         // charFields[3] = Hs

double Hn[3];            // Hn[0]=H1, Hn[1]=H2 and Hn[2]=H3

// Initialize the output file
std::ofstream outfile;
outfile.open("fit_parameters.txt", std::fstream::out);
outfile << "H0"<< '\t'
      << "Hso"<< '\t'
      << "Hi"<< '\t'
      << "Hs"<< '\t'
      << "error"<< '\t'
      << "Rsquared"<< std::endl;
outfile.close();
```

```
// Initialize the another output file
std::ofstream outfile2;
outfile2.open("fit_parameters_rsquared.txt",
                std::fstream::out);
outfile2 << "H0"<< '\t'
      << "Hso"<< '\t'
      << "Hi"<< '\t'
      << "Hs"<< '\t'
      << "error"<< '\t'
      << "Rsquared"<< std::endl;
outfile2.close();

// Read in the experimental data from file "datafile.txt"
std::ifstream datafile;
datafile.open("datafile.txt", std::fstream::in);
i=0;
while(datafile >> expH[i] >> expDeltaR[i]){
   i++;
}
datafile.close();
if(expH[0] == 0.){
   expH[0] += .00000001;       // Remove singularity at H=0
}
numDataPoints = i;
p=0;
for(total=0, p=0; p<numDataPoints; p++){
```

```
    expDeltaR[p] *= -1.; // My input files have deltaL = -deltaR
    total += expDeltaR[p];
}

mean = total / numDataPoints;

// Read in limits for fit
std::ifstream limits;
limits.open("limits.txt", std::fstream::in);
limits >> minH0 >> maxH0 >> minHso >> maxHso
       >> minHi >> maxHi >> minHs >> maxHs >> maxErr;
limits.close();

lowErr=maxErr;
highRSquared = 0;

// Step through possible values based on Min, Max and Step Sizes
for(j=(minH0/stepH0); j<=(maxH0/stepH0); j++){
    charFields[0] = (j * stepH0);
    for(k=(minHso/stepHso); k<=(maxHso/stepHso); k++){
        charFields[1] = (k * stepHso);
        for(l=(minHi/stepHi); l<=(maxHi/stepHi); l++){
            charFields[2] = (l * stepHi);
            for(m=(minHs/stepHs); m<=(maxHs/stepHs); m++){
                charFields[3] = (m * stepHs);
```

```
// Set the Hn paramters from the charFields at each step
Hn[0] = ( charFields[0] + charFields[1]
      + charFields[3] );
Hn[1] = ( (4./3.)  * charFields[1]
      + (2./3.)  * charFields[3]
      + charFields[2] );
Hn[2] = ( 2.  * charFields[3]
      + charFields[2] );


ssErr = 0;
ssTot = 0;
bigErr = 0;
outfile.open("fit_parameters.txt",
       std::fstream::out |std::fstream::app);
outfile2.open("fit_parameters_rsquared.txt",
       std::fstream::out |std::fstream::app);
for(n=0; n<numDataPoints; n++){
   fit = deltaR (expH[n], Hn);
   pointErr = pow((fit - expDeltaR[n]),2);
   meanErr = pow((mean - expDeltaR[n]),2);
   ssErr += pointErr;
   ssTot += meanErr;
}
rSquared = 1 - (ssErr / ssTot);
if(ssErr < maxErr){
   outfile << charFields[0] << '\t'
```

```
                        << charFields[1] << '\t'
                        << charFields[2] << '\t'
                        << charFields[3] << '\t'
                        << ssErr << '\t'
                        << rSquared << std::endl;
                    lowErr=ssErr;
                }
                outfile.close();
                if(rSquared > highRSquared){
                    outfile2 << charFields[0] << '\t'
                        << charFields[1] << '\t'
                        << charFields[2] << '\t'
                        << charFields[3] << '\t'
                        << ssErr << '\t'
                        << rSquared << std::endl;
                    highRSquared=rSquared;
                }
                outfile2.close();
            }
        }
    }
}
```

APPENDIX F

MATHEMATICA NOTEBOOK FOR DATA ANALYSIS

deltaL[H_]:=

$-\frac{e^2}{2\pi^2 \text{hbar}}$(PolyGamma[$\frac{1}{2}+\frac{\text{H0+Hso+Hs}}{H}$] − PolyGamma[$\frac{1}{2}+\frac{\frac{4}{3}\text{Hso}+\frac{2}{3}\text{Hs+Hi}}{H}$]+

$\frac{1}{2}$(PolyGamma[$\frac{1}{2}+\frac{\text{2Hs+Hi}}{H}$] − PolyGamma[$\frac{1}{2}+\frac{\frac{4}{3}\text{Hso}+\frac{2}{3}\text{Hs+Hi}}{H}$]))

hbar $= 1.05457 * 10^{-34}$;

$e = 1.60 * 10^{-19}$;

vf $= 1.39 * 10^{6}$;

lstNone = Import["/home/jmeans/deltaRfits/2007_05_01_600mK_78A_none.txt", "tsv"];

plotNone = ListPlot[lstNone];

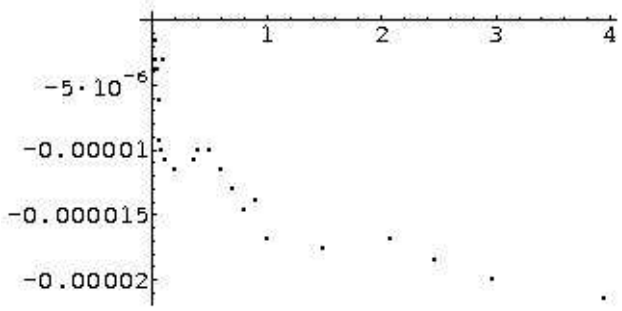

H0 = 13;

Hso = 1;

Hi = 0.015;

Hs = 0.0055;

plotNoneFit = Plot[deltaL[H], {H, 0, 4}];

Show[plotNone, plotNoneFit, {Frame → True}];

$\tau 0 = \sqrt{\frac{\text{hbar}}{2e\text{vf}^2\text{H0}}}$

$\tau \text{so} = \frac{\text{hbar}}{2e\text{vf}^2\tau 0\ \text{Hso}}$

$\tau \text{i} = \frac{\text{hbar}}{2e\text{vf}^2\tau 0\ \text{Hi}}$

$\tau s = \frac{\text{hbar}}{2 e v f^2 \tau 0 \, Hs}$

$\text{Diff} = \frac{v f^2 \tau 0}{2}$

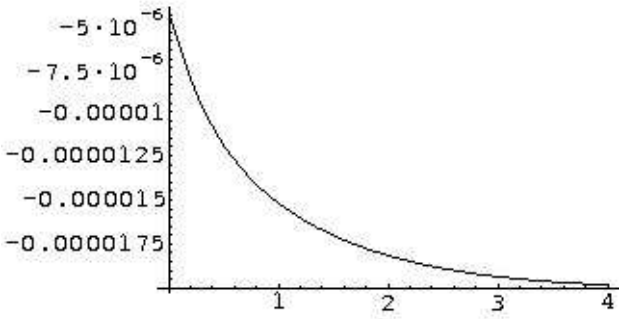

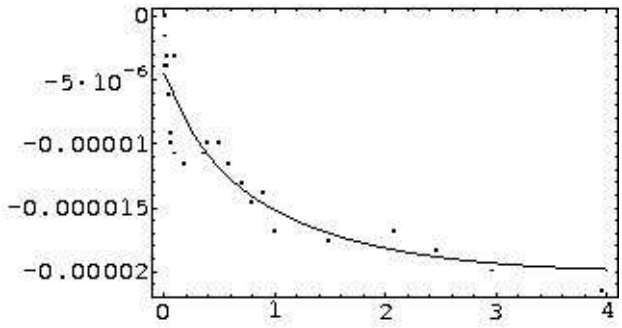

3.62223×10^{-15}

4.7089×10^{-14}

3.13927×10^{-12}

8.56164×10^{-12}

0.00349926

```
fitNone = Table[deltaL[H], {H, 0.0001, 4, 0.0001}];
lstWith = Import["/home/jmeans/deltaRfits/2007_05_01_600mK_78A_with.txt", "tsv"];
plotWith = ListPlot[lstWith, {PlotJoined → False}];
```

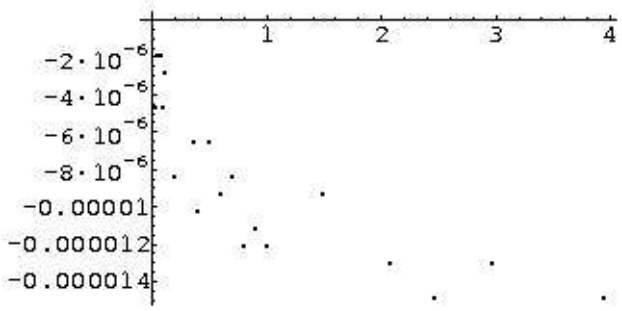

$\mathbf{H0} = 5.5;$

$\mathbf{Hso} = .71;$

$\mathbf{Hi} = 0.0135;$

$\mathbf{Hs} = .0105;$

$\mathbf{plotWithFit} = \mathbf{Plot}[\mathbf{deltaL}[H], \{H, 0, 4\}];$

$\mathbf{Show}[\mathbf{plotWith}, \mathbf{plotWithFit}, \{\mathbf{Frame} \rightarrow \mathbf{True}\}];$

$\tau\mathbf{0} = \sqrt{\frac{\mathbf{hbar}}{2\mathbf{evf}^2\mathbf{H0}}}$

$\tau\mathbf{so} = \frac{\mathbf{hbar}}{2\mathbf{evf}^2\tau\mathbf{0}\,\mathbf{Hso}}$

$\tau\mathbf{i} = \frac{\mathbf{hbar}}{2\mathbf{evf}^2\tau\mathbf{0}\,\mathbf{Hi}}$

$\tau\mathbf{s} = \frac{\mathbf{hbar}}{2\mathbf{evf}^2\tau\mathbf{0}\,\mathbf{Hs}}$

$\mathbf{Diff} = \frac{\mathbf{vf}^2\tau\mathbf{0}}{2}$

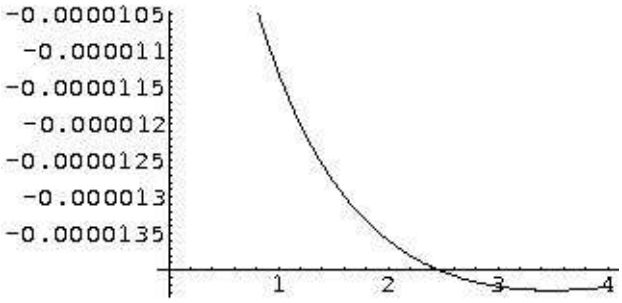

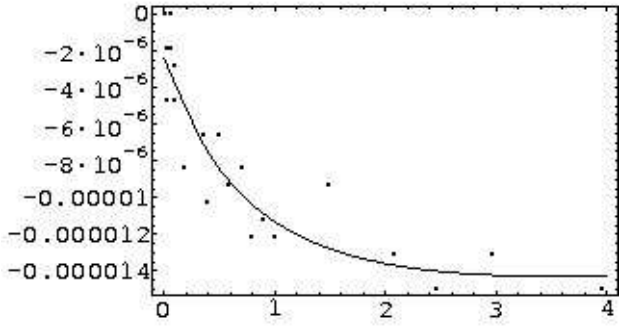

5.56886×10^{-15}

4.31391×10^{-14}

2.2688×10^{-12}

2.91702×10^{-12}

0.0053798

fitWith $=$ **Table**[**deltaL**[H], {H, 0.0001, 4, 0.0001}];

Export["**/home/jmeans/deltaRfits/2007_05_01_600mK_78A_none_fit.txt**", **fitNone**, "**tsv**"];

Export["**/home/jmeans/deltaRfits/2007_05_01_600mK_78A_with_fit.txt**", **fitWith**, "**tsv**"];

FitXAxis $=$ **Table**[i, {i, 0.0001, 4, 0.0001}];

Export["**/home/jmeans/deltaRfits/40000points.csv**", **FitXAxis**, "**tsv**"];

APPENDIX G

ADDITIONAL EXPERIMENTAL DATA

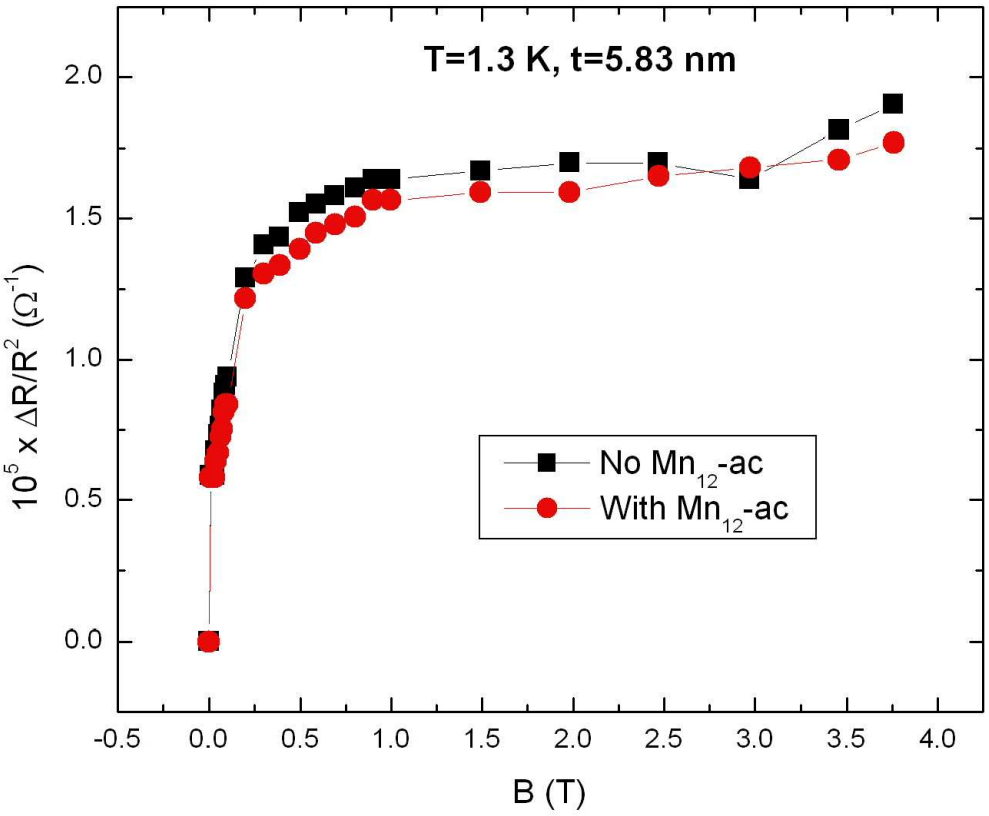

Figure 25: Magnetoresistance of 5.83 nm Au film at 1.3 K.

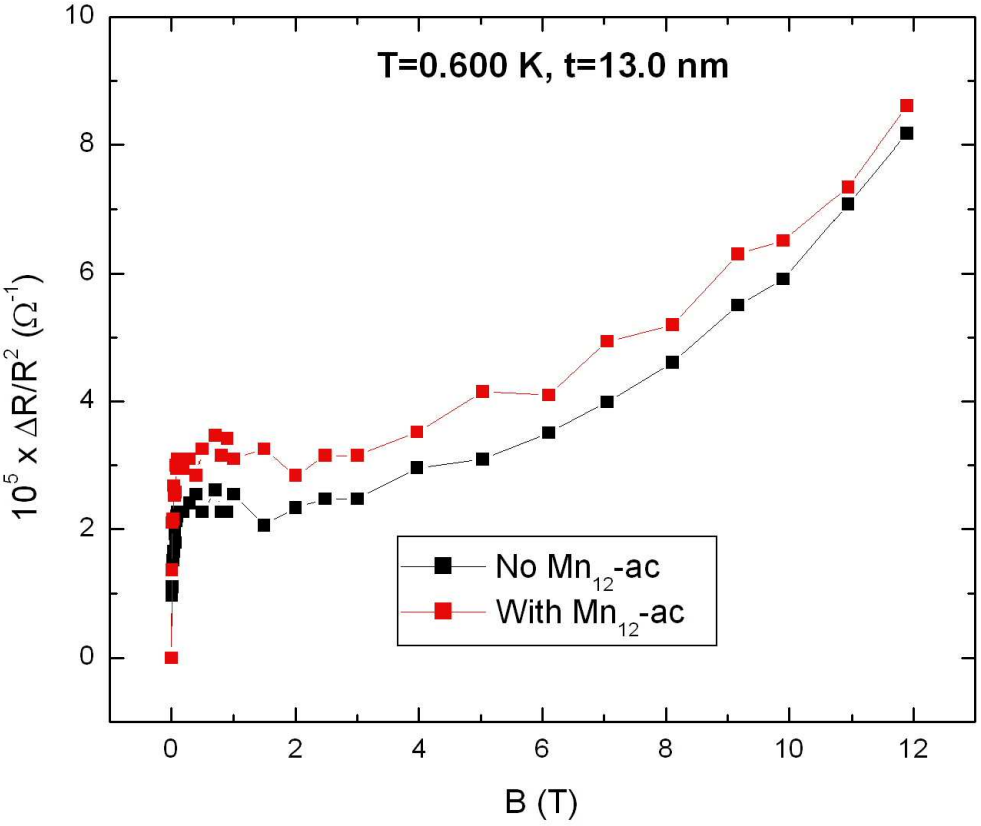

Figure 26: Magnetoresistance of 13.0 nm Au film at 600 mK.

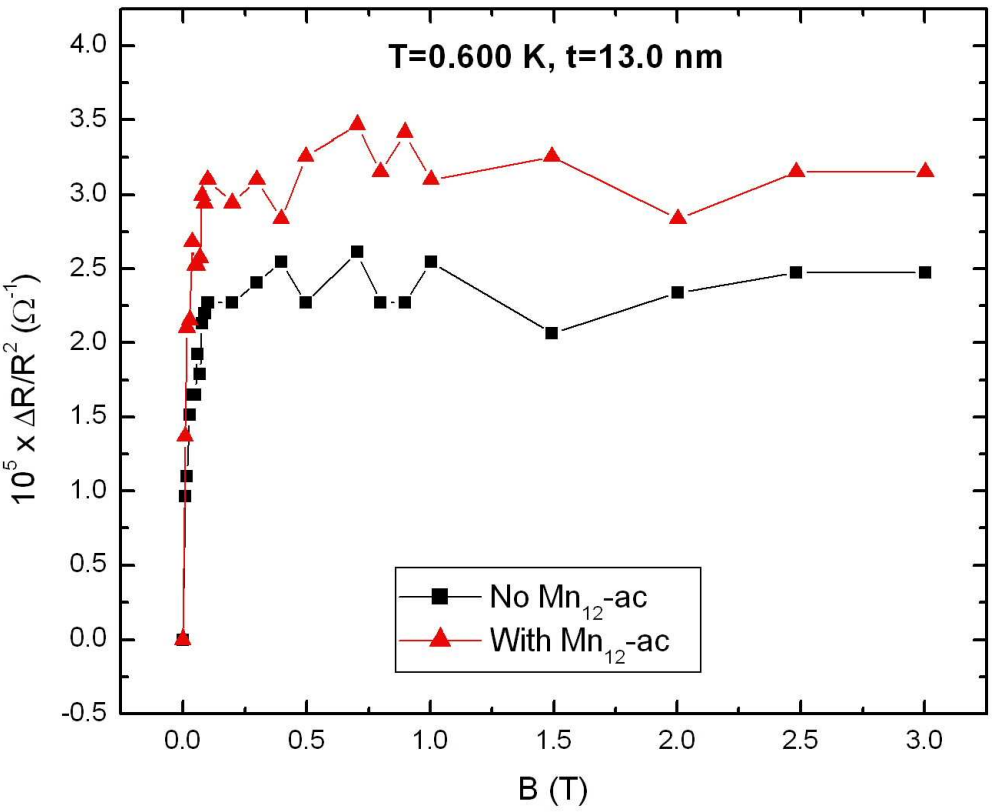

Figure 27: Magnetoresistance of 13.0 nm Au film at 600 mK, low-field portion.

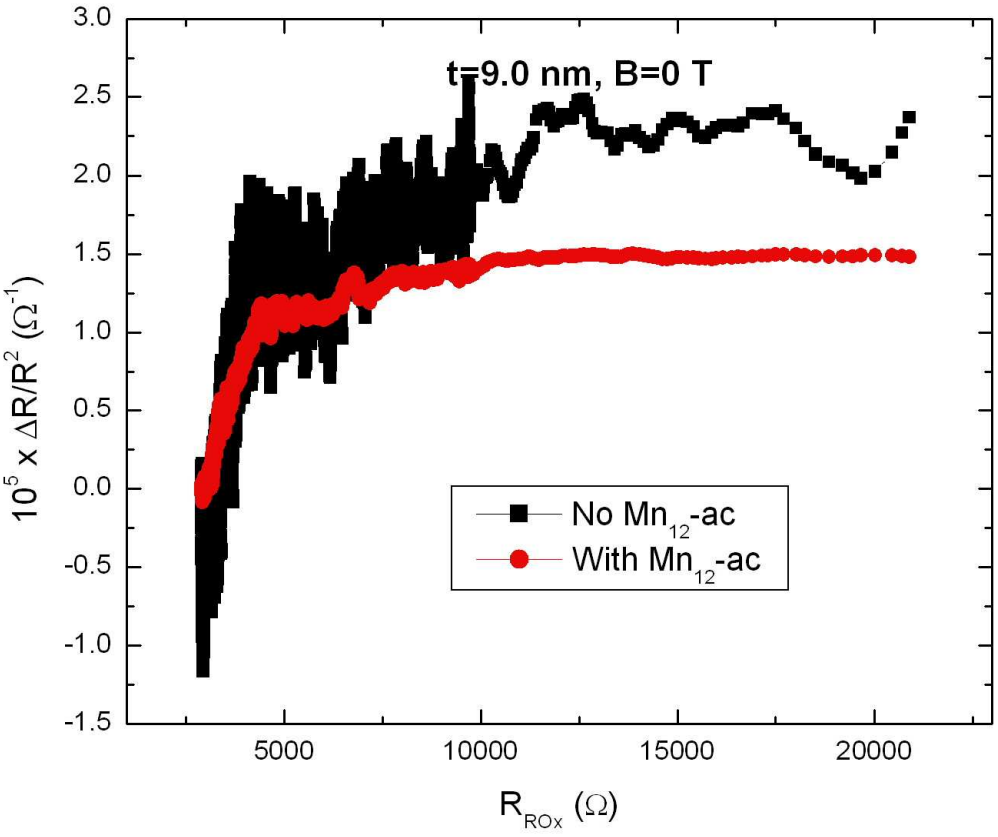

Figure 28: Temperature dependence of resistance of 9.0 nm Au film at B = 0 T (raw data). Note that a resistance of $\sim$3130 Ω corresponds to 3 K, the blocking temperature for Mn_{12}–ac. Lower noise in the measurement with Mn_{12}–ac data is due to the use of two different lock-in amplifiers for the two measurements.

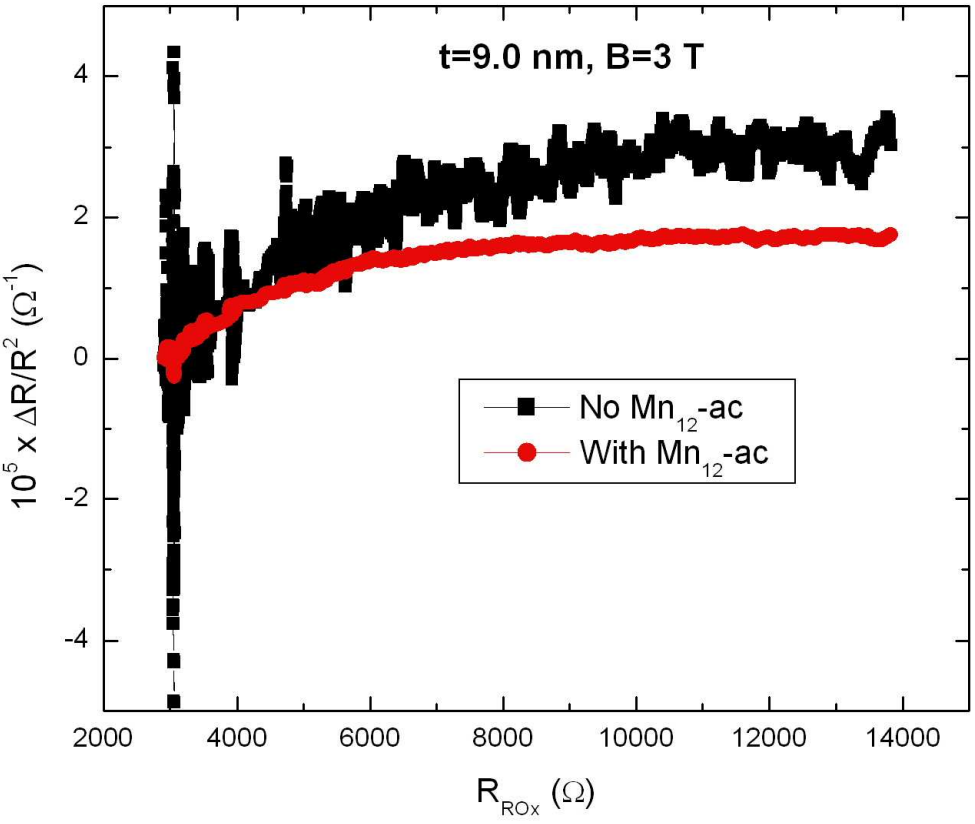

Figure 29: Temperature dependence of resistance of 9.0 nm Au film at B = 3 T (raw data). Note that a resistance of $\sim$3130 Ω corresponds to 3 K, the blocking temperature for Mn_{12}–ac. Lower noise in the measurement with Mn_{12}–ac data is due to the use of two different lock-in amplifiers for the two measurements.

APPENDIX H

TEMPERATURE CALIBRATION

Figure 30 shows the standard curve for the Lake Shore Cryotronics Ruthenium Oxide thermometer (model #RX-202A, serial #U01955). The plot was created using data given on the Lake Shore website (http://www.lakeshore.com). The thermometer used in the experiments presented in this dissertation was not calibrated, so this standard curve was used. The model RX-202A sensor has an accuracy of ± 30mK at 500 mK versus the standard curve.

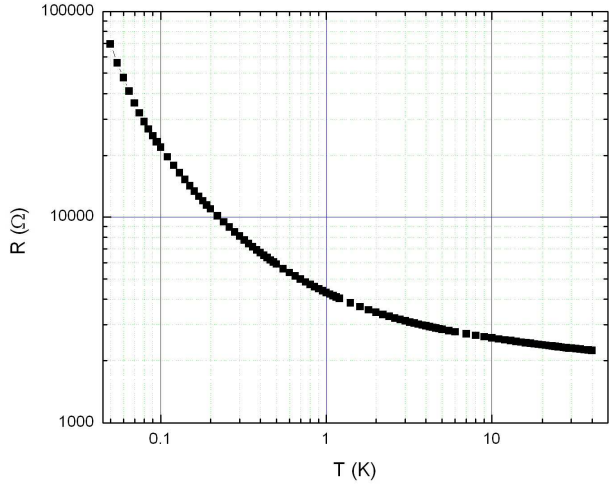

Figure 30: Standard R-T curve for ROx thermal resistor.

VITA

Joel Lewis Means received his Bachelor of Science degree in physics and mathematics from Harding University in Searcy, AR, in May 1999. He entered the Physics program at Texas A&M University in September 2001, and received his Doctor of Philosophy degree in December 2007. Dr. Means can be reached by contacting Dr. Winfried Teizer, Dept. of Physics, Texas A&M University, TAMU 4242, College Station, TX 77843-4242.